Shock Waves (2010) 20:217–239
DOI 10.1007/s00193-010-0249-z

ORIGINAL ARTICLE

Simulation of impulse effects from explosive charges containing metal particles

K. Balakrishnan · D. V. Nance · S. Menon

Received: 3 December 2009 / Revised: 15 March 2010 / Accepted: 17 March 2010 / Published online: 13 April 2010

Abstract The propagation of an explosive blast wave containing inert metal particles is investigated numerically using a robust two-phase methodology with appropriate models to account for real gas behavior, inter-phase interactions, and inter-particle collisions to study the problem of interest. A new two-phase Eulerian–Lagrangian formulation is proposed that can handle the dense nature of the flow-field. The velocity and momentum profiles of the gas and particle phases are analyzed and used to elucidate the inter-phase momentum transfer, and its effect on the impulsive aspects of heterogeneous explosive charges. The particles are found to pick up significant amounts of momentum and kinetic energy from the gas, and by virtue of their inertia, are observed to sustain it for a longer time. The impulse characteristics of heterogeneous explosives are compared with a homogeneous explosive containing the same amount of high explosive, and it is observed that the addition of solid particles augments the impulsive loading significantly in the near-field, and to a smaller extent in the far-field. The total impulsive loading is found to be insensitive to the particle size added to the explosive charge above a certain cut-off radius, but the individual impulse components are found to be sensitive, and particles smaller than this cut-off size deliver about 8% higher total impulse than the larger ones. Overall, this study provides crucial insights to understand the impulsive loading characteristics of heterogeneous explosives.

Communicated by F. Zhang.

K. Balakrishnan · S. Menon (✉)
School of Aerospace Engineering, Georgia Institute of Technology,
270 Ferst Drive, Atlanta, GA 30332-0150, USA
e-mail: suresh.menon@aerospace.gatech.edu

D. V. Nance
AFRL/RWPC, 101 W. Eglin Blvd. STE 334,
Eglin AFB, FL 32542-6810, USA

Keywords Detonation · Blast wave · Heterogeneous explosive · Impulsive loading · Multiphase flow

1 Introduction

Heterogeneous explosives are formed by the addition of solid metal particles to a charge of a high explosive. The detonation of a heterogeneous explosive results in the interplay of several fluid-mechanic and thermodynamic parameters, thereby complicating the underlying physics of the problem. When a heterogeneous explosive charge is detonated, it gives rise to an outward moving blast wave that attenuates due to the effects of spreading. At the same time, the solid particles pick up momentum from the gas due to drag (both viscous and pressure drag) and are set into motion, trailing behind the blast wave. This momentum transfer from the gas to the particles can be classified into two phases: the momentum transfer from the gas to the particles during the detonation wave passage; and that due to the flow behind the detonation wave. For small and/or light particles, the former can be more significant and provide the primary acceleration mechanism at the early time instants. Furthermore, due to the dense nature of the flow-field, the dynamic compaction results in inter-particle interactions in the form of collisions and direct contact, which is the other driver of the particles at early times. Subsequently, the particles, owing to their inertia, attain a constant terminal velocity, and sustain it until they catch-up with the attenuating leading blast wave. Some of the leading particles penetrate the leading blast wave into the ambient air, and then slow down due to aerodynamic drag, allowing for the leading blast wave to again re-overtake the particle front. Of preponderant interest is the total deliverable impulsive loading from such a heterogeneous charge. The total impulse at any location from the charge will be due to both

the gas and the particles, with the particles being the dominant contributor in the near-field. However, the inter-phase momentum transfer, inter-particle collisions, and their effect on the impulsive loading is not properly understood, and this study is aimed at investigating and elucidating the same.

Studies of the aforementioned physical phenomena are limited, but there has been some experimental and numerical investigations that have provided some valuable insights. The detonation of a heterogeneous explosive charge is characterized by a detonation velocity deficit in comparison with a homogeneous charge, as observed in experiments undertaken by Lee et al. [1], due to the associated momentum and energy transfer. Lanovets et al. [2] performed a numerical study based on a two-fluid approach and reported that for a certain range of particle size and density, the solid particles can catch-up with the shock front and overtake it. Milne [3] developed a mesoscale model to study detonation of a nitromethane charge with inert particles using a simple one step Arrhenius kinetics, and explained the increase in detonation failure diameter with particle size for small inert particles. Zhang et al. [4] carried out experimental and numerical studies to obtain the shock front and the particle cloud trajectory for a nitromethane charge containing steel particles. They found that for spherical and cylindrical charges, the possibility of the solid particles overtaking the shock front exists, but is highly unlikely for planar charges due to their lower attenuation rates. They also noted that the distance required for the large particles to overtake the shock front strongly depends on the charge size and material density, but weakly on the solid volume fraction. They also concluded that a particle size limit exists, above which the distance required for the particles to penetrate the shock front is less sensitive to the particle size, and below which, the distance required depends on particle size. In another study, Zhang et al. [5] reported that the momentum transfer from an explosive to the solid particles during the particle crossing of the detonation front is insignificant for heavy-metal and significant for light-metal particles.

Some joint experimental and numerical efforts have also been undertaken to evaluate impulsive loading from a heterogeneous charge comprising of a high explosive and inert/reacting solid particles. Frost et al. [6] carried out a combined experimental and numerical study focusing on particle momentum and impulse effects of a nitromethane charge with steel particles. They showed that the integrated particle momentum flux is larger than the gas momentum flux by a factor of about 3–4 in the near field, and the impulsive load on a near-field structure was increased by a factor of 2 for a heterogeneous charge, when compared to a homogeneous charge. Massoni et al. [7] proposed a reactive model for aluminized explosive charges in spherical coordinates. They combined an ALE method and a detonation tracking technique, and matched blast wave parameters with experiments for aluminized explosive charges. Ripley et al. [8] numerically obtained velocity and temperature transmission factors, defined as the ratio of velocity and temperature, respectively, of particle to the gas as the detonation wave crosses the particle in a heterogeneous explosive. They identified three different regimes of interest, i.e., when the particle size is much smaller, comparable to, and much larger than the reaction zone thickness. Although the aforementioned studies have provided some useful insights to the complex physics involved in the problem under study, more investigation is required to understand the impulsive loading aspects from the detonation of heterogeneous explosives. The transient nature of the components of the impulsive loading (i.e., due to gas pressure, gas momentum and solid momentum fluxes) has not been addressed by the past studies. Furthermore, the effect of early-stage inter-particle collisions on the later-stage particle distribution and deliverable impulsive loading requires more detailed investigation.

In the present study, the primary interest is to understand the blast effects from a heterogeneous explosive charge using a two-phase formulation. Very recently, we studied the problem of homogeneous explosive charges and the associated impulse effects, with scaling laws for the shock overpressure and impulsive loading provided for different explosives [9]. In another recent study, we reported the effects of mixing and hydrodynamic instabilities behind explosive blast waves due to dilute reactive particle clouds [10]. Building on these foundations, we hereby extend our investigation to dense heterogeneous explosives and the associated impulsive loading aspects. In the current study, during the initial stage of the detonation the particle loading is considered dense and this effect has to be included in the modeling. Multiphase flow modeling is not straightforward due to two primary reasons: (1) the presence of non-conservative terms, also called "nozzling" terms due to their being analogous to one-dimensional flow in a variable area duct such as a nozzle [11,12]; (2) requirement of appropriate closure for interface pressure and velocity. To overcome these difficulties, we use an approach similar to the Discrete Equations Method (DEM), originally proposed by Abgrall and Saurel [13] for dense particle phase modeling within a two-fluid approach. The scheme is robust in nature and can handle shock interactions with volume fraction discontinuities. The basic idea behind the DEM is the treatment of volume fraction as a piece-wise continuous variable, and the evaluation of the inter-cell interfaces using distinctive Riemann problems with pure material on either side. Chinnayya et al. [14] extended the DEM to study detonation waves in heterogeneous energetic materials. Their methodology used the pure material equations of state, instead of a mixture equation of state, highlighting the robust nature of the DEM. Le Metayer et al. [15] extended the DEM to handle evaporation fronts. A similar approach has been independentally developed by others [16,17].

In the original DEM used by all these authors, the gas and solid phases were treated Eulerian in nature. In the current approach, the solid particles are tracked using Lagrangian tracking (to be discussed later), and this requires an extension of the DEM to an Eulerian–Lagrangian formulation. We have chosen the use of a Lagrangian approach for the solid particles as this enables the precise computation of particle trajectories. The differences between the original Eulerian–Eulerian DEM and the presently developed Eulerian–Lagrangian DEM are also highlighted in this paper.

This study is aimed at providing insights into the fundamental physics of detonation processes in heterogeneous explosives, dense particle modeling and dispersion, with a focus on inert particles. This paper is organized as follows: in Sect. 2, the governing equations and the numerical methodology are discussed. In Sect. 3, the results and discussions are presented for the multiphase blast wave problem, and the underlying physics elucidated. Finally, in Sect. 4, the conclusions drawn from this study are presented.

2 Governing equations and numerical method

2.1 Gas phase

The gas phase Navier–Stokes equations, applicable in dense two-phase flows in the absence of body forces are [11–14,17]

$$\begin{aligned}
&\frac{\partial}{\partial t}\begin{bmatrix} \alpha_g\rho_g \\ \alpha_g\rho_g u_{g,i} \\ \alpha_g\rho_g E_g \\ \alpha_g\rho_g Y_{g,k} \end{bmatrix} + \frac{\partial}{\partial x_j}\begin{bmatrix} \alpha_g\rho_g u_{g,j} \\ \alpha_g\rho_g u_{g,i}u_{g,j} + \alpha_g p_g\delta_{ij} \\ \alpha_g\left(\rho_g E_g + p_g\right)u_{g,j} \\ \alpha_g\rho_g Y_{g,k}u_{g,j} \end{bmatrix} \\
&+\frac{\partial}{\partial x_j}\begin{bmatrix} 0 \\ -\alpha_g\tau_{g,ij} \\ -\alpha_g u_{g,i}\tau_{g,ji} + \alpha_g q_{g,j} \\ \alpha_g\rho_g Y_{g,k}V_{g,j} \end{bmatrix} \\
&= \begin{bmatrix} 0 \\ p^*\frac{\partial\alpha_g}{\partial x_j}\delta_{ij} - {\tau_{ij}}^*\frac{\partial\alpha_g}{\partial x_j} \\ p^*u_j{}^*\frac{\partial\alpha_g}{\partial x_j} - {u_i}^*{\tau_{ij}}^*\frac{\partial\alpha_g}{\partial x_j} \\ \dot{\omega}_k \end{bmatrix} + \begin{bmatrix} \dot{\rho}_p, \\ \dot{F}_{p,i}, \\ \dot{Q}_p + \dot{W}_p, \\ \dot{S}_{p,k}, \end{bmatrix} \qquad (1)
\end{aligned}$$

where α_g denotes the gas phase volume fraction, ρ_g the density, $u_{g,i}$ the ith Cartesian component of velocity, E_g the total specific energy given by the sum of the internal (e_g) and kinetic energies, $e_g + \frac{1}{2}u_{g,i}u_{g,i}$, and $Y_{g,k}$ the mass fraction of the kth species. The stress tensor is denoted by $\tau_{g,ij}$, the j-direction heat flux by $q_{g,j}$, the j-component diffusion velocity by $V_{g,j}$, and the chemical production of the kth species by $\dot{\omega}_k$. Since the problem of interest involves high speed flow, the diffusion time scales are generally at least an order of magnitude higher than the convective time scales. Thus, the diffusion terms, viz. $q_{g,j}$, $\tau_{g,ij}$ and $V_{g,j}$ are neglected in this study, following previous approaches [4,12]. However, viscosity and thermal conductivity play a role in the computation of the inter-phase interaction terms (also called coupling terms or relaxation terms).

In Eq. (1), p^* and ${u_i}^*$ denote respectively, the pressure and ith component of velocity at the interface between the two phases. The interface stress tensor is denoted by ${\tau_{ij}}^*$, and is neglected using the same assumption that diffusion time scales are large for the present problem under study. The last term on the right hand side identifies the inter-phase coupling terms: mass transfer $\dot{\rho}_p$, ith component momentum transfer $\dot{F}_{p,i}$, heat transfer $\dot{Q}_p$, work transfer $\dot{W}_p$, and chemical production of kth species $\dot{S}_{p,k}$. These terms are evaluated using Lagrangian tracking of solid particles, and are discussed shortly. The problem under study is characterized by high pressures and densities, and thus the use of the perfect gas equation of state for the detonation products will not accurately predict the behavior of the flow-field. To this end, explosives are modeled using a real gas assumption. Although many real gas models exist in literature, we use the Jones–Wilkins–Lee (JWL) equation of state for the detonation products in this study. The JWL equation of state is further simplified by using the constant specific heat at constant volume (C_v) approach [18] to obtain a thermal form of the equation of state, given as

$$p_g = A\,\exp\left(\frac{-R_1\rho_o}{\rho_g}\right) + B\,\exp\left(\frac{-R_2\rho_o}{\rho_g}\right) + \omega\rho_g C_v T_g, \qquad (2)$$

where T_g denotes the gas temperature; A, B, R_1, R_2 and ω denote JWL constants, and ρ_o, the explosive density [19]. The JWL equation of state becomes asymptotic to the perfect gas equation of state at low densities.

Since the problem under study involves a high speed flow, a shock capturing scheme is essential to accurately capture the blast wave and the discontinuities involved in the flow-field. Here, we use the MUSCL (Monotone Upstream-centered Schemes for Conservation Laws) approach [20], due to its well established robustness. For computing the fluxes at inter-cell interfaces, we use the HLLC approximate Riemann solver [20]. Since we do not use a grid aligned along the Cartesian axes, the approach of Batten et al. [21] is used to compute the HLLC fluxes, applicable for a generic grid. Several canonical studies have been undertaken to study the ability of the solver to handle discontinuities. In particular, the classical Sedov's point explosion [20] and appropriate problems from [22] have been considered, not presented here for brevity. The solver predicts sharp interfaces; in particular, shocks are captured with about three cells, and contact surfaces with about five cells, which we believe is reasonable with the MUSCL approach. Furthermore, the Discrete Equations Method (DEM) [13–15] is used to account for

the dense particle loading, and will be discussed in detail in Sect. 2.3.

2.2 Solid phase

For the solid phase, Lagrangian tracking is used to compute the particle velocity vector ($u_{p,i}$) from the forces acting on a particle. Since the number of particles to be tracked can be very large under some scenarios, the concept of parcel is employed [23]. Here, a parcel represents a group of particles, each corresponding to the same position and velocity vectors, and temperature. The number of parcels is chosen based upon various factors such as computational cost and available memory, while the number of particles assigned to a parcel is chosen based upon the desired volume fraction/mass loading. The particle position vector ($x_{p,i}$) is obtained from the velocity vector. These equations are summarized below for the circumstance involving no inter-phase mass transfer:

$$\frac{dx_{p,i}}{dt} = u_{p,i}, \tag{3}$$

$$m_p \frac{du_{p,i}}{dt} = \frac{\pi}{2} {r_p}^2 C_D \rho_g |u_{g,i} - u_{p,i}| \left(u_{g,i} - u_{p,i}\right) - \frac{4}{3}\pi {r_p}^3 \frac{\partial p_g}{\partial x_i} + m_p A_{c,i}, \tag{4}$$

where m_p is the particle mass, r_p is the particle radius, and $A_{c,i}$ is the i-component of net acceleration/deceleration on a particle due to inter-particle collisions [23,24]. The particle mass m_p is obtained as $4/3\pi {r_p}^3 \rho_p$, where ρ_p is the solid particle material density. In the above equation, C_D represents the effective drag coefficient and is usually expressed as an empirical function of Reynolds number (Re), Mach number (M) and solid volume fraction (α_p). Several different drag laws have been proposed in literature, each being unique to a specific multiphase problem. To the best of our knowledge, no universally accepted drag law available in literature is applicable for all kinds of multiphase problems, e.g., dilute and dense particle fields or high and low speed flow. Thus, we will use different drag laws for different problems in this paper, depending on the regime of application. In Eq. (4), we have neglected other forces acting on the particles, such as Saffman lift, Magnus lift, gravity, Basset force and Coriolis effects [25], based on an order of magnitude analysis. Most of these terms were also neglected in the numerical analysis undertaken in [4] of the heterogeneous explosive problem currently under study.

Due to the dense nature of the problem, the inter-particle interaction has to be accounted for. To this end, Snider's collision model [23,24] is used to compute the inter-particle collision acceleration/deceleration ($A_{c,i}$). This inter-particle collision acceleration/deceleration is as a result of the constant collision/contact between particles, which cannot be neglected for the high solid volume fractions involved in the problem under study. This term arises due to the dynamic compaction of the flow-field in the vicinity of the solid particles. More details on the physics of dynamic compaction can be found elsewhere [11,26]. For the collision/contact model used in this study (and in [23,24]), the stress due to inter-particle collision is obtained as an empirical function of the solid volume fraction only, similar to the approaches used in [11,26]. Other researchers have used an empirical model where the granular-stress is a function of both the solid volume fraction and solid material density [12,27]. In the present study, the model proposed by [23,24] is chosen, as this is applicable for an Eulerian–Lagrangian formulation, unlike the others mentioned.

The stress due to inter-particle interaction is generally high when the particle cloud is dense, as the interactions between contiguous particles are more pronounced for denser clouds. As the particle cloud expands outwards, the cloud density decreases, thereby resulting in fewer inter-particle interactions. Subsequently, as the solid particles have significantly expanded outwards, the particle cloud tends to the dilute limit (in terms of solid volume fraction), and the inter-particle interaction becomes negligible. These physical interactions are accounted for in the present model by an empirical function of the solid volume fraction, α_p. In the collision/contact model used, the inter-particle force is obtained from the inter-particle stress (τ) given by [23,24]

$$\tau = \frac{P_s {\alpha_p}^{\beta}}{\alpha_{cs} - \alpha_p}, \tag{5}$$

where P_s (units of pressure) and β are model coefficients, and α_{cs} is the solid volume fraction at close packing. The particle acceleration/deceleration due to inter-particle collision is obtained as a gradient of the inter-particle stress using the equation

$$A_{c,i} = -\frac{1}{\alpha_p \rho_p} \frac{\partial \tau}{\partial x_i}. \tag{6}$$

In this inter-particle collision/contact model, the inter-particle stress and acceleration are assumed to be independent of particle size and velocity, as done so in other models [11,12,26,27]. The heat transfer between the two phases is estimated assuming only convection and neglecting radiation, and is used to obtain the particle temperature (T_p)

$$m_p C_p \frac{dT_p}{dt} = 2\pi r_p \kappa_g Nu \left(T_g - T_p\right), \tag{7}$$

where C_p is the specific heat of the solid particle and κ_g is the thermal conductivity of the gas phase. The Nusselt number (Nu) is typically expressed as empirical functions of Reynolds number and Prandtl number in the literature. We have neglected other terms in the particle temperature equation like the "added mass" and the "history integral" terms [28]. The particle–particle collision model could, in

theory, also play a role in the particle temperature equation. Particle collisions can cause velocity fluctuations, and this can give rise to the so called "granular temperature." This granular temperature is due to shear in particle collisions, during which energy dissipation can occur due to inelastic collisions [25]. This effect is neglected for the time being, with the assumption that convection is the only dominant heat transfer mechanism between the two phases. The system of governing equations for the solid phase are solved using a fourth order Runge-Kutta scheme to obtain the solid particle position vector, velocity vector and temperature.

The coupling terms that appear on the right side of the gas phase governing equations, Eq. (1) are obtained by volume averaging over all the particles/parcels in a finite volume (Vol) and are summarized as follows (without mass transfer)

$$\dot{F}_{p,i} = \frac{1}{Vol}\sum_{n=1}^{N} n_{p,n}\left[\frac{\pi}{2}r_{p,n}^2 C_{D,n}\rho_{g,n}|u_{p,i,n}-u_{g,i,n}| \times \left(u_{p,i,n}-u_{g,i,n}\right)+\frac{4}{3}\pi r_{p,n}^3\frac{\partial p_{g,n}}{\partial x_i}\right], \tag{8}$$

$$\dot{Q}_p = \frac{1}{Vol}\sum_{n=1}^{N} n_{p,n}\left[2\pi r_{p,n}\kappa_{g,n}Nu_n\left(T_{p,n}-T_{g,n}\right)\right], \tag{9}$$

$$\dot{W}_p = \frac{1}{Vol}\sum_{n=1}^{N} n_{p,n}\left[\frac{\pi}{2}r_{p,n}^2 C_{D,n}\rho_{g,n}|u_{p,i,n}-u_{g,i,n}| \times \left(u_{p,i,n}-u_{g,i,n}\right)u_{p,i,n}+\frac{4}{3}\pi r_{p,n}^3\frac{\partial p_{g,n}}{\partial x_i}u_{p,i,n}\right], \tag{10}$$

where N is the total number of parcels in a finite volume cell and n_p is the number of particles per parcel. The subscript n is used to denote the nth particle; when used for a gas-phase variable, it represents the value of the gas-phase variable at the location of the nth particle. Equation (10) involves a repetition of the tensor index i, and is thus obtained as a summation of three terms (in three dimensions). Since no inter-phase mass transfer is assumed in this study, $\dot{\rho}_p$ and $\dot{S}_{p,k}$ are neglected in Eq. (1).

2.3 Discrete equations method (DEM)

2.3.1 Formulation

The problem under study involves the presence of a dense cloud of solid particles where finite volumes are occupied by both phases, thereby necessitating the use of a multiphase model. To this end the Discrete Equations Method (DEM) [13–15] is used in the present study—a robust multiphase method well suited for multiphase flows involving shocks and solid particles. The basic idea behind the method starts with the representation of the volume fraction field as piecewise continuous, typical in any Godunov scheme. This is shown in Fig. 1 for three cells containing different number of particles, and therefore different volume fractions, before applying the MUSCL reconstruction, i.e., first order representation.

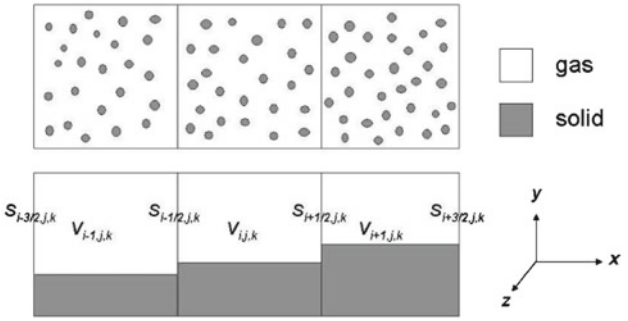

Fig. 1 Volume fraction field representation in DEM. The schematic shows how a discrete particle field can be represented as a piecewise continuous volume fraction variable for flux computation

Following the methodology outlined in [13,14], we derive the DEM approach in three dimensions, although it was originally proposed in two dimensions. First we derive the approach applicable for a Cartesian grid, and later extend to non-Cartesian grids. While the original DEM proposed by Abgrall and Saurel [13] is Eulerian for both the carrier and dispersed phases, the current research effort involves the extension of the Eulerian–Eulerian (EE) DEM to an Eulerian–Lagrangian (EL) formulation. In our formulation, since the exact distribution of particles in space is known at every time instant due to the Lagrangian tracking of the particles, we do not need a separate volume fraction equation as used in the EE DEM. Thus, the solid volume fraction, α_p, is obtained by volume averaging each finite volume cell; the gas volume fraction field is then obtained as $\alpha_g = 1-\alpha_p$. In addition, our approach differs from [13,14] in the sense that we use the DEM approach to only compute the gas-phase fluxes, as the solid-phase is solved for by means of Lagrangian tracking. Moreover, we treat the solid phase to be incompressible in the EL DEM. The gas-phase governing equations at the microscopic scale in 3D can be summarized as:

$$\frac{\partial W}{\partial t}+\frac{\partial F}{\partial x}+\frac{\partial G}{\partial y}+\frac{\partial H}{\partial z}=0, \tag{11}$$

where

$$W = \left(\rho_g, \rho_g u_g, \rho_g v_g, \rho_g w_g, \rho_g E_g, \rho_g Y_k\right)^T,$$
$$F = \left(\rho_g u_g, \rho_g {u_g}^2 + p_g, \rho_g u_g v_g, \rho_g u_g w_g, \left(\rho_g E_g + p_g\right)u_g, \rho_g u_g Y_k\right)^T,$$
$$G = \left(\rho_g v_g, \rho_g u_g v_g, \rho_g {v_g}^2 + p_g, \rho_g v_g w_g, \left(\rho_g E_g + p_g\right)v_g, \rho_g v_g Y_k\right)^T,$$

$$H = \Big(\rho_g w_g,\, \rho_g u_g w_g,\, \rho_g v_g w_g,\, \rho_g {w_g}^2 + p_g,\, \big(\rho_g E_g + p_g\big) w_g,\, \rho_g w_g Y_k\Big)^T, \tag{12}$$

for the continuity, x-momentum, y-momentum, z-momentum, energy and kth species equations, respectively.

We define an indicator function, λ, that takes the value 1 in regions of gas, and 0 otherwise. Following [14], this function obeys the equation

$$\frac{\partial \lambda}{\partial t} + u^* \frac{\partial \lambda}{\partial x} + v^* \frac{\partial \lambda}{\partial y} + w^* \frac{\partial \lambda}{\partial z} = 0, \tag{13}$$

where u^*, v^* and w^* denote respectively, the local interface velocities in the x, y and z directions. This equation vanishes for points within either of the phases, and is non-vanishing only at points located at multiphase interfaces. Combining these equations by integrating in time and space, results in the following for a cell C_{ijk}:

$$\begin{aligned}
&\int_0^{\Delta t} \int_{C_{ijk}} \left(\frac{\partial(\lambda W)}{\partial t} + \frac{\partial(\lambda F)}{\partial x} + \frac{\partial(\lambda G)}{\partial y} + \frac{\partial(\lambda H)}{\partial z} \right) \mathrm{d}V\, \mathrm{d}t \\
&= \int_0^{\Delta t} \int_{C_{ijk}} \left((F - u^* W) \frac{\partial \lambda}{\partial x} + (G - v^* W) \frac{\partial \lambda}{\partial y} \right. \\
&\quad \left. + (H - w^* W) \frac{\partial \lambda}{\partial z} \right) \mathrm{d}V\, \mathrm{d}t,
\end{aligned} \tag{14}$$

where $\mathrm{d}V = \mathrm{d}x\, \mathrm{d}y\, \mathrm{d}z$. In the above equation, the left-hand side denotes the conservative fluxes, and the right-hand side denotes the non-conservative fluxes. The non-conservative terms arise only at multiphase interfaces and are obtained from the uniform interface velocity assumption, and will be (for a Cartesian grid)

$$\begin{aligned}
F - u^* W &= \big(0,\, p^*,\, 0,\, 0,\, p^* u^*,\, 0\big)^T, \\
G - v^* W &= \big(0,\, 0,\, p^*,\, 0,\, p^* v^*,\, 0\big)^T, \\
H - w^* W &= \big(0,\, 0,\, 0,\, p^*,\, p^* w^*,\, 0\big)^T.
\end{aligned} \tag{15}$$

The above expression is strictly valid only when no interphase mass transfer is involved. When mass transfer is to be accounted for, the procedure outlined in [15] is better suited.

The different integrals from Eq. (14) that need to be evaluated are:

$$\begin{aligned}
I_1 &= \int_0^{\Delta t} \int_{C_{ijk}} \frac{\partial(\lambda W)}{\partial t} \mathrm{d}V\, \mathrm{d}t \\
I_2 &= \int_0^{\Delta t} \int_{C_{ijk}} \frac{\partial(\lambda F)}{\partial x} \mathrm{d}V\, \mathrm{d}t
\end{aligned} \tag{16}$$

$$I_3 = \int_0^{\Delta t} \int_{C_{ijk}} \big(F - u^* W\big) \frac{\partial \lambda}{\partial x} \mathrm{d}V\, \mathrm{d}t$$

for the temporal term, x-direction conservative and non-conservatives, respectively, and similar expressions for fluxes in the y and z directions. For the remainder of the formulation, we present these expressions only for the x-direction fluxes, with the expressions being similar in mathematical form for the y- and z-directions. Following the approach outlined in [14], these integrals can be approximated as

$$\begin{aligned}
I_1 &= \int_{C_{ijk}} \Big((\lambda W)^{n+1} - (\lambda W)^n \Big)\, \mathrm{d}V \\
&= \Big((\lambda W)_{ijk}{}^{n+1} - (\lambda W)_{ijk}{}^n \Big)\, \Delta x \Delta y \Delta z,
\end{aligned} \tag{17}$$

for the temporal term and

$$\begin{aligned}
I_2 &= \int_0^{\Delta t} \int_{z_{k-1/2}}^{z_{k+1/2}} \int_{y_{j-1/2}}^{y_{j+1/2}} \int_{x_{i-1/2}}^{x_{i+1/2}} \frac{\partial(\lambda F)}{\partial x} \mathrm{d}V\, \mathrm{d}t \\
&= \int_0^{\Delta t} \int_{z_{k-1/2}}^{z_{k+1/2}} \int_{y_{j-1/2}}^{y_{j+1/2}} \big((\lambda F)_{i+1/2} - (\lambda F)_{i-1/2} \big)\, \mathrm{d}S\, \mathrm{d}t,
\end{aligned} \tag{18}$$

for the x-direction conservative flux, where $\mathrm{d}S = \mathrm{d}y\, \mathrm{d}z$. To compute I_2, the flux is obtained as a surface average. Observing Fig. 1, it is deduced that the inter-cell interface at $i + 1/2$ and $i - 1/2$ can be constructed as a series of smaller interfaces, i.e., three out of four different possible scenarios, viz. gas–gas ($g - g$), gas–solid ($g - s$), solid–gas ($s - g$) and solid–solid ($s - s$), where 'gas–solid' refers to a state of gas on the left and solid on the right. This is made possible due to the piecewise representation of the volume fraction field. The total gas flux passing through the surface area at $i + 1/2$ or $i - 1/2$ is obtained as a summation over each of these smaller interfaces. For instance, at $i - 1/2$, the total flux integrated from $j - 1/2$ to $j + 1/2$ and $k - 1/2$ to $k + 1/2$ is obtained as follows

$$\begin{aligned}
&\int_{z_{k-1/2}}^{z_{k+1/2}} \int_{y_{j-1/2}}^{y_{j+1/2}} (\lambda F)_{i-1/2} \mathrm{d}S \\
&= {\lambda^*}_{i-1/2} {F^*}_{i-1/2} (g - g) S_{g-g} \\
&\quad + {\lambda^*}_{i-1/2} {F^*}_{i-1/2} (g - s) S_{g-s} \\
&\quad + {\lambda^*}_{i-1/2} {F^*}_{i-1/2} (s - g) S_{s-g} \\
&\quad + {\lambda^*}_{i-1/2} {F^*}_{i-1/2} (s - s) S_{s-s},
\end{aligned} \tag{19}$$

where the subscripts g and s denote the gas and solid, respectively. We introduce the '*' superscript to denote interface quantities. Here, λ^* denotes the indicator function, which is obtained from the sign of the interface velocity (u^*); the interface surface areas S_{g-g}, S_{g-s}, etc. are obtained using

Table 1 Conservative flux at cell interface $i-1/2$

Contact type	Contact surface	Indicator function, λ
Gas–gas	$S\min(\alpha_{i-1},\alpha_i)$	1
Gas–solid	$S\max(\alpha_{i-1}-\alpha_i,0)$	1 if $u^*\geq 0$; 0 otherwise
Solid–gas	$S\max(\alpha_i-\alpha_{i-1},0)$	1 if $u^*<0$; 0 otherwise
Solid–solid	$S\min(1-\alpha_{i-1},1-\alpha_i)$	0

the gas volume fraction. These expressions are summarized in Table 1 for the cell interface at $i-1/2$, where S denotes the inter-cell area, α is the gas volume fraction, and u^* is the interface velocity. Note that the last row of Table 1 corresponds to the solid phase on both sides of the interface; the indicator function is zero as no gas flux can flow through the interface with solid on either side.

At gas–solid contacts, the indicator function is based on the sign of the interface velocity, which decides whether the flux of gas is permissible through the local interface. For conservative fluxes, the gas flux can be flowing either inside or outside the cell, depending on the sign of the indicator function. When the multiphase interface is blocking the flow of gas, the indicator function is zero. Note that the conservative flux consists of the convective and the pressure fluxes; since they are together computed from the Riemann solver, the sign of the interface velocity decides whether or not both fluxes have to be computed. The underlying reason behind the splitting of the cell interfaces into different pairs in the flux computation with the DEM is that the Riemann problem is different when gas exists on both sides of the interface, as opposed to gas on one side and solid on the other. If a pressure wave approaches an interface, part of the momentum and energy is reflected and part of it transmitted; the exact amounts that are reflected and transmitted will be different when the interface consists of gas on either side, or gas on one side and solid on the other. This is due to different compressibilities of the two phases under consideration, and thus the splitting of cell interfaces into a combination of different Riemann problems, as first proposed in the EE DEM [13], is essential to accurately use the appropriate Riemann solver in the evaluation of the total flux crossing the cell interface.

The same approach for flux computation is used at the location $i+1/2$. The y- and z-direction conservative fluxes are similar in form to I_2 and are thus not shown here for brevity. To obtain the non-conservative flux I_3, we use the following expression

$$I_3=\int_0^{\Delta t}\int_{z_{k-1/2}}^{z_{k+1/2}}\int_{y_{j-1/2}}^{y_{j+1/2}}\Big[\big(F-u^*W\big)_{i-1/2}[\lambda]_{i-1/2}+\big(F-u^*W\big)_{i+1/2}[\lambda]_{i+1/2}\Big]\,\mathrm{d}S\,\mathrm{d}t$$

$$+\int_0^{\Delta t}\int_{z_{k-1/2}}^{z_{k+1/2}}\int_{y_{j-1/2}}^{y_{j+1/2}}\big(F-u^*W\big)_i[\lambda]_i\,\mathrm{d}S\,\mathrm{d}t, \tag{20}$$

where the subscripts $i-1/2$ and $i+1/2$ denote the multiphase interfaces at the cell boundary, and i denotes the internal interfaces; the boundary and internal terms are evaluated separately. Following the approach outlined in [14], the non-conservative term at $i-1/2$ is evaluated as

$$\int_{z_{k-1/2}}^{z_{k+1/2}}\int_{y_{j-1/2}}^{y_{j+1/2}}\big(F-u^*W\big)_{i-1/2}[\lambda]_{i-1/2}\mathrm{d}S$$
$$=[\lambda^*]_{i-1/2}\big(F^*-u^*W^*\big)_{i-1/2}(s-g)S_{s-g}$$
$$+[\lambda^*]_{i-1/2}\big(F^*-u^*W^*\big)_{i-1/2}(g-s)S_{g-s}. \tag{21}$$

In the above expression, $[\lambda^*]$ represents the jump in the indicator function, and is summarized in Table 2 at the cell interface $i-1/2$. The same approach is used to compute the non-conservative term at $i+1/2$. Note that at the cell interface $i-1/2$, the non-conservative flux will have to be computed for the cell i only if the multiphase interface velocity (u^*) is positive; otherwise, it has to be computed for the cell $i-1$. Furthermore, the non-conservative flux will be computed at the interface $i+1/2$ for the cell i only if the interface velocity is negative; otherwise it will be computed for cell $i+1$. These terms in the y- and z-directions are similar in form to I_3 and are thus not shown here for brevity.

To compute I_3, the only term that remains to be addressed is the last integral in Eq. (20), which corresponds to internal interfaces–these terms represent the relaxation/coupling terms. The significance of the relaxation terms are that when the two phases are not in mechanical or thermal equilibrium, the relaxation terms tend to drive the flow-field such that the two phases tend toward equilibrium, albeit with finite time scales. In the EE DEM, the non-conservative fluxes at the internal interfaces (relaxation terms) were computed by using the Riemann solver and summing up over all the internal interfaces [14]. Our formulation differs from the EE DEM in the sense that we also consider viscous effects, i.e., the total drag (viscous + pressure) and heat transfer, for which we use empirical correlations (Sect. 2.2). In doing so, we can account for spherical particles inside the finite volume, unlike the original EE DEM, which was formulated for square particles [14]. One similarity between the evaluation of these

Table 2 Non-conservative flux at cell interface $i - 1/2$

Contact type	Contact surface	Jump in indicator function, [λ]
Gas–gas	$S\min(\alpha_{i-1}, \alpha_i)$	0
Gas–solid	$S\max(\alpha_{i-1} - \alpha_i, 0)$	-1 if $u^* \geq 0$; 0 otherwise
Solid–gas	$S\max(\alpha_i - \alpha_{i-1}, 0)$	1 if $u^* \geq 0$; 0 otherwise
Solid–solid	$S\min(1 - \alpha_{i-1}, 1 - \alpha_i)$	0

terms between the EE DEM and the EL DEM is that they are obtained as a summation over all the particles present in a given cell.

2.3.2 Interface closure

Since the flux estimation in DEM involves knowledge of the interface velocity precisely (refer to Tables 1, 2), only contact surface based Riemann solvers, such as the HLLC and the Roe scheme [20] can be used; in the current study, we use the HLLC Riemann solver for flux estimation. While the inter-cell flux is obtained in the conventional way at gas–gas contacts, for the gas–solid contacts we solve a half-Riemann problem [29], due to the incompressible solid assumption. By a half-Riemann problem, we refer to a condition when the shock or rarefaction propagates only on one side of the inter-cell interface, i.e., the side of the gas. Since the solid particles are incompressible, the interface velocity at gas–solid contacts is equated to the mass-weighted average velocity of all the solid particles in the cell corresponding to the side of the solid, given as

$$u_i{}^* = \frac{\sum_{n=1}^{N} m_{p,n} u_{p,i,n}}{\sum_{n=1}^{N} m_{p,n}}. \tag{22}$$

This is obtained from the assumption that continuity in velocity exists near gas-solid contacts. The conservative and non-conservative fluxes at multiphase contacts are computed using this solid particle velocity based interface velocity. When all the particles in a cell have the same mass, the interface velocity is the arithmetic average of all the solid particle velocities. Although we will investigate only mono-disperse particle size distributions in this study, the current formulation can be easily extended to handle a varying particle size distribution. This is made possible by using an appropriate particle mass (dependent on size) for each particle in a cell in the mass-weighting computation of $u_i{}^*$ (Eq. 22).

For the non-conservative flux computation, both interface pressure and velocity needs to be known, as can be perceived from Eq. (15). We have demonstrated the interface velocity computation (Eq. 22); now we present the interface pressure computation. The interface pressure (p^*) is obtained accordingly, depending on a compression or rarefaction at the two-phase interface. Comparing the velocities of the gas and solid particles, it can be deduced whether the interface corresponds to a state of compression or rarefaction. For compression, the interface pressure is obtained using shock and Rankine–Hugoniot relations; for rarefaction, isentropic relations and Riemann invariants are used. These expressions are summarized in Appendix A. Thus, two equations are solved numerically to obtain two variables, i.e., interface pressure and density, with the interface velocity known. Once the interface variables have been computed, the conservative and non-conservative fluxes can be evaluated following the DEM approach. Another approach to obtain the interface pressure, more simpler in nature, is the use of an acoustic analogy [14]. For a multiphase interface with gas to the left and solid to the right, the acoustic analogy gives the expression for the interface pressure (assuming incompressible solid) $p^* = p_l - \rho_l c_l (u_l - u^*)$, where the variable c denotes the speed of sound, and the subscript l denotes the left gas state. On the other hand, the corresponding acoustic analogy expression for a multiphase interface with gas to the right and solid to the left will be $p^* = p_r + \rho_r c_r (u_r - u^*)$, where the subscript r denotes the right gas state. Very recently, the effect of using different interface pressure closures in the EE DEM was addressed [30].

2.3.3 Non-cartesian grids

The DEM formulation presented until now is applicable only for a Cartesian grid; we now discuss the modifications involved to extend the formulation to non-Cartesian grids. For a grid not aligned along the Cartesian axes, the interface velocity is the contravariant velocity (denoted hereafter as q^*), and is obtained at the gas–solid contact as $q^* = u_i{}^* n_i$, where n_i denotes the direction cosines of the outward normal at the interface. This is analogous to obtaining the left and right velocities in the pure-gas (single phase) Riemann solver, in which the direction cosines of the outward normal are used to estimate the interface velocity using the left and right velocity components [21]. From the same reference for the single phase Riemann solver, variables q_l and q_r are defined as $q_l = u_l n_x + v_l n_y + w_l n_z$ and $q_r = u_r n_x + v_r n_y + w_r n_z$, where the subscripts l and r denote the left and right states, respectively; u, v and w denote respectively, the velocity components in x, y and z; n_x, n_y and n_z represent the direction cosines of the outward normal at the interface in x, y and z, respectively. Subsequently, the authors of [21] use q_l and q_r in the Riemann solver so as to obtain the flux at an interface for the single phase Riemann problem, whose outward

normal is not aligned to the regular Cartesian directions. The flux function for the HLLC Riemann solver applicable for a generic grid is slightly different, as outlined in [21]. We have extended the same approach to define the interface velocity at gas-solid contacts for the Riemann solver in the two-phase problem with the formula $q^* = u_p n_x + v_p n_y + w_p n_z$, where u_p, v_p and w_p denote respectively, the x, y and z components of the solid particle velocity obtained from mass-weighted averaging (Eq. 22). For any generic grid, the conservative fluxes (Table 1) are obtained using the HLLC Riemann solver as outlined in [21]. The mathematical expression of the conservative HLLC flux function is the same at gas–gas and gas–solid contacts, but the only difference being the definition of the interface velocity, q^* at the type of the contact. For a gas-gas contact, q^* is obtained from the Riemann solver, while for a gas-solid contact, it is obtained from mass-weighted averaging of the solid particle velocities (Eq. 22).

It is noteworthy of mention that a half-Riemann problem at a gas–solid contact can be treated to be equivalent to a full-Riemann problem with the solid state replaced with a modified 'ghost' gas state with the same pressure and density as the side of the gas, but with the negative of the velocity augmented with twice the solid velocity. Substituting these left and right states in the HLLC interface velocity equation, it can be easily shown that the interface velocity for this modified Riemann problem equals the solid velocity, even for a non-Cartesian grid.

For the non-conservative flux computation applicable for a non-Cartesian grid, the computation of Eq. (20) is not trivial as the integrand is in a non-conservative form. However, in our formulation we compute this term only at the cell boundaries, i.e. not in the interior, which simplifies the computation. We use the interface pressure and interface velocity to compute the non-conservative fluxes. For a grid not aligned along the Cartesian axes, the non-conservative fluxes are obtained as $p^* n_x$, $p^* n_y$ and $p^* n_z$, respectively for the x, y and z momentum equations [16]. For the energy equation, the corresponding non-conservative flux will be $p^* q^*$, where, as mentioned before, q^* is obtained as $q^* = u_p n_x + v_p n_y + w_p n_z$. This is analogous to the consideration of three surface areas Sn_x, Sn_y and Sn_z at an inter-cell interface whose surface area is S, aligned along x, y and z directions, respectively. The non-conservative fluxes are computed at each of these three interfaces, multiplied by the appropriate surface areas and the jump in the indicator functions (see Table 2), and then included in the finite volume methodology. This term, which is Eq. (20) evaluated at the boundary will be $(0, p^* n_x, p^* n_y, p^* n_z, p^* q^*, 0)^T [\lambda](S\Delta\alpha)$, in 3D for the continuity, x, y, and z momentum, energy and kth species equations, respectively. The rules for obtaining $[\lambda]$ and $(S\Delta\alpha)$ are summarized in Table 2. Note that $[\lambda] = +1$ or -1 decides whether the flux is entering or leaving the cell.

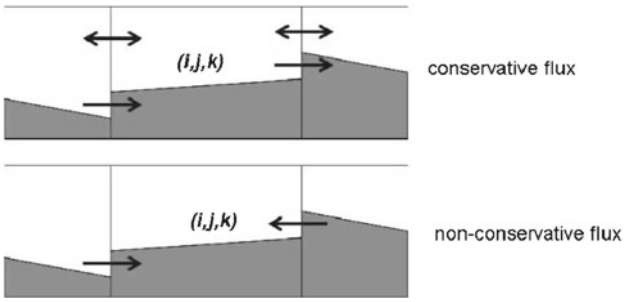

Fig. 2 When to compute conservative and non-conservative fluxes for cell (i, j, k). The arrow denotes the direction the interface has to move to have a non-zero gas flux entering or leaving the middle cell. The *white regions* denote the space available for the gas; the *grey regions* denote the space occupied by the solid particles

2.3.4 Summary

To summarize this formulation, Fig. 2 shows the volume fraction representation across three contiguous cells. The arrows denote the direction to which the interface has to move so that the gas-phase flux needs to be computed for the middle cell. For interfaces with gas on either side, the conservative flux is non-zero for any direction of the movement of the interface. For interfaces with gas on one side, and solid on the other, the conservative flux is non-zero if and only if the interface moves in a direction such that the flow of gas is permissible (either entering or leaving the cell). Furthermore, the non-conservative fluxes are non-zero if and only if the gas-solid contact moves in a direction such that the cell-interface is not blocked. Note that the arrow directions shown for the non-conservative flux in Fig. 2 are applicable only for cell (i, j, k); if the arrows are reversed for the non-conservative flux computation shown in Fig. 2, these terms will not be accounted for cell (i, j, k), but will be considered for the other cells $(i - 1, j, k)$ or $(i + 1, j, k)$, as the case may be. The rules outlined in Table 1 are used for computing the conservative fluxes, and those in Table 2 to compute the non-conservative fluxes.

The DEM approach is used to compute the fluxes in all the three directions, i.e., x, y and z. To compute the fluxes in y, the cells aligned along the y directions, i.e., $(i, j - 1, k)$, (i, j, k) and $(i, j+1, k)$ are considered and the piecewise linear representation of the volume fraction field (using MUSCL) is constructed along the y-direction this time. The same methodology mentioned hitherto is used this time to compute the fluxes in the y-direction, similarly for the fluxes in the z-direction. Thus, the piecewise linear representation of the volume fraction field is so constructed, depending on whether the flux computation is along x-, y- or z-direction. Furthermore, due to the presence of a volume fraction gradient within the cell (due to MUSCL reconstruction), an additional term has to be included in the finite volume formulation [13]. This term arises in the computation of the non-conservative

flux for the second-order scheme due to the presence of a volume fraction gradient within the cell. This term (in x-direction) is computed using the gas volume fractions to the immediate left of the $i + 1/2$ interface and to the right of the $i - 1/2$ interface, which are obtained from MUSCL reconstruction. The origin of this term and its precise mathematical form are well explained in [30].

The major advantage of the EL DEM over the EE DEM is that the treatment of the dispersed phase to not be in continuum, enables the precise estimation of particle trajectories. However, the EL DEM suffers a major drawback over its counterpart. The EL DEM will not be applicable to multiphase problems where $\alpha_p \rightarrow 1$, since this would violate continuum assumption required for flux computation and equation of state usage. Thus, the EL DEM is not suited for multiphase simulations such as liquid jet breakup, under water explosions, shock bombardment into compressible materials, etc. For these problems, the EE DEM is better suited. Problems involving α_p less than, say 0.7, such as the problem under investigation, and the problem of detonation propagation through a dense cloud of solid particles are well suited for study with the EL DEM. For the proper application of EL DEM, the maximum allowable value of α_p is currently under investigation.

2.4 Initial detonation profile

The initial detonation profiles are obtained based on a one-dimensional simulation employing the Gas-Interpolated-solid-Stewart-Prasad-Asay (GISPA) method for the detonation process [31]. This method permits time-accurate simulation of detonation from the time of the initial shock through the completion of the explosive burn. The GISPA method is robust, as emphasized by its ability to capture the reaction zone as well as the Von Neumann spike. In the GISPA method, the Euler equations are solved in a one-dimensional radial coordinate system using the progress variable approach [32]. We have extended the same method to include solid particles, along with appropriate reaction rates and equations of state for the condensed explosive and the detonation product gases. Recently [9], we have applied the GISPA method to study detonations in homogeneous explosives, and have provided some critical validation studies of our algorithm.

The initialization of the detonation profile within the initial charge is critical to the problem under study. This process is complicated by the fact that our detonation algorithm is not yet adapted for dense collections of metal particles. In order to achieve a proper initialization, we must compensate for this theoretical shortfall. We propose two approaches as remedies for this problem: (i) based upon the limited availability of data, we may scale the pure explosive detonation conditions by appropriate factors, especially for the particles, or (ii) we may scale the detonation energy based upon the ratio of the mass of energetic material to metal mass. The former method tends to work well if there is a sufficient body of data; the latter method is robust and more generally applicable. Since there is very little data available for heterogeneous explosives at the onset of detonation, we have chosen to implement method (ii) for this study.

The detonation initialization based on the GISPA method differs from other ways of initialization, such as "programmed burn" [33], and constant volume explosion [4]. In a programmed burn, the detonation wave speed must be known a priori, and is usually a function of the detonation wave curvature. In the constant volume explosion initialization, the flow field is assumed constant inside the explosive charge, and so the early momentum transfer from the gas to the particles can be erroneous. On the other hand, the GISPA algorithm is based on first principles, and therefore, the initialization is expected to be more realistic.

The initial detonation profiles as predicted by the GISPA algorithm, corresponding to a 11.8 cm diameter explosive charge comprising of Nitromethane (NM) and 463 μm steel particles, initially occupying 62% by volume of the charge (as used in [4]) is shown in Fig. 3 as the detonation wave reaches the outer periphery of the charge. Also shown are the profiles for a homogeneous 11.8 cm diameter NM charge for comparison. As observed, the pressure and velocity profiles for the heterogeneous charge (NM/Fe) show a deficit as compared with the homogeneous charge (NM), due to the absorption of momentum and energy by the particles in the former. Furthermore, the particles are also observed to attain a significant velocity, albeit lower than the gas. Based on a numerical study presented by Ripley et al. [8], the velocity transmission factor (defined as the ratio of the particle to gas velocities as the detonation wave crosses the particle) is about 0.42 when the particle size is comparable to the reaction zone, and is about 0.34 when the particle size is much larger, both corresponding to a volume fraction of 62%. Interestingly, the ratio of the peak solid particle velocity as predicted by the GISPA algorithm to the gas velocity at the Chapman–Jouguet (CJ) point is in this range. It is also interesting to note that the Taylor wave behind the leading detonation front is observed to cause flow reversal (gas) near ∼0.03 m radial location for the NM/Fe charge.

Since the GISPA uses a progress variable approach, the detonation products are treated as a single species. Subsequently, the one-dimensional detonation profiles from the GISPA are extrapolated to the three-dimensional grid, and the detonation products are replaced by a mixture of CO, N_2, H_2O and H_2, with their mass-fractions obtained from the balanced chemical equation CH_3NO_2 (nitromethane) $\rightarrow CO + \frac{1}{2} N_2 + H_2O + \frac{1}{2}H_2$.

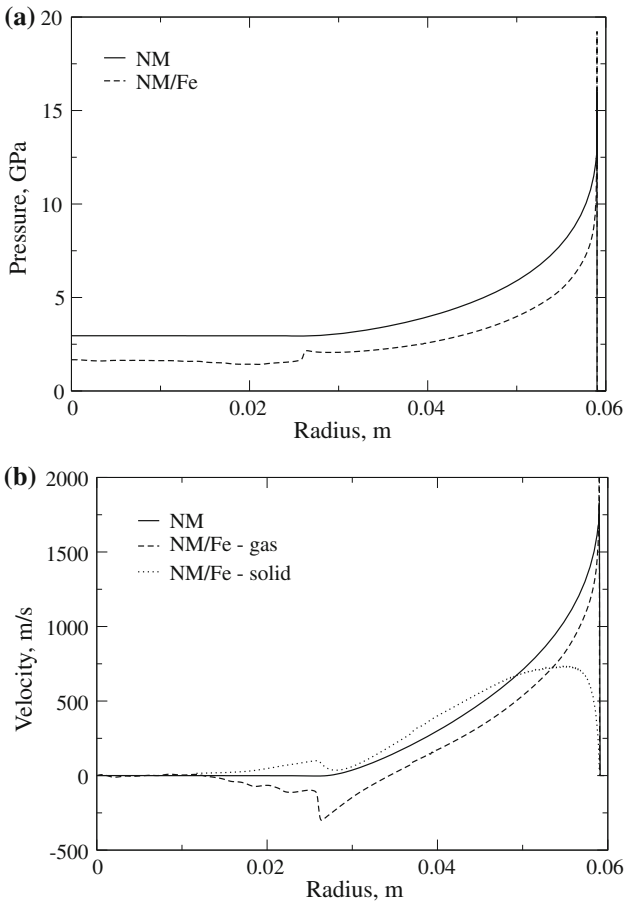

Fig. 3 Initialization for the detonation simulations involving homogeneous (NM) and heterogeneous (NM/Fe) explosive charges: **a** pressure and **b** velocity

3 Results and discussion

The simulation code is a well established solver suited for DNS/LES of combustion/turbulent multiphase flows [9,10,34]. The solid phase solver, DEM and the JWL equation of state are new additions to the hydrocode, and thus, many canonical studies have been completed to establish the accuracy of the new algorithms. Some key results of these studies are presented in Appendix B.

3.1 Detonation in a heterogeneous explosive

Detonation studies from the experiments of Zhang et al. [4] are simulated here. A heterogeneous charge of 11.8 cm dia. containing nitromethane and steel particles is considered. A range of particle sizes are studied. For the initial study, steel particles of 463 μm dia, randomly distributed and occupying 62% of the total charge volume is studied. Simulations are carried out using a spherical sector grid 2.4 m long (r), and 20° in the azimuth (θ) and zenith (ϕ) directions, with a grid resolution of $1000 \times 10 \times 10$. Other grid resolutions have also been considered, and the results were similar. We use free-slip boundary conditions along the azimuth and zenith directions, and a supersonic outflow at the outer plane. The drag law and Nusselt number correlations of Akhatov and Vainshtein [27] are used for this study. This drag law predicts a drag coefficient (C_D) dependent on α_p and Reynolds number, Re; our computations show that C_D is as high as 4 for the particles in the near-field owing to the dense nature of the flow, and decreases to $0.42 - 0.5$ in the far-field as the flow transitions to the dilute regime.

The Snider's model [23,24] coefficient, P_s is chosen as 500 MPa, based on an order of magnitude analysis comparing collision and drag forces on a particle (see further discussions below). For the solid volume fraction range applicable to the current study, the chosen value of P_s (500 MPa) results in inter-granular stresses lower than the ultimate strength of steel, i.e., the maximum stress that steel can withstand before rupturing. Moreover, the inter-granular stress predicted by this model for the problem is in the range obtained by material researchers [35], who measured the intergranular stress by tensile straining carbon steels. The parameters $\beta = 3$ [23] and $\alpha_{cs} = 0.9$ are chosen for the collision model.

The blast wave, the particle front trajectory, and the shock overpressure are shown in Fig. 4, and the results are in good agreement with experimental data. Also shown is the overpressure obtained from a homogeneous charge (NM) containing the same amount of high explosive as this heterogeneous charge (NM/Fe). As observed, the momentum and energy transfer to the particles results in a decrease in the overpressure for the heterogeneous charge. It is observed that the particles at the leading edge of the cloud attain a velocity of around 1300 m/s in about 0.1 ms, and subsequently maintain a constant terminal velocity. At around 0.9 m and 0.6 ms, the particle cloud front is observed to overtake the shock wave, and subsequently the leading particles slow down.

To understand the significance of using the JWL equation of state to model explosives, another simulation was undertaken incorporating the perfect gas equation of state. With this approximation, the leading blast wave was faster, and the shock overpressure higher, than that otherwise predicted with the use of the JWL equation of state, not shown for brevity. Thus, for the remainder of the study, the explosive simulations are undertaken with the JWL equation of state to model the behavior of detonation products.

To illustrate the flow topography, the sector grid showing the gas pressure contour and the location of the particles at 0.38 and 0.98 ms are shown in Fig. 5. The particles lag behind the blast wave at the earlier time, but some of them have overtaken the blast wave at the latter time. The front of the particle cloud is not a sharp interface due to the initial random distribution of the particles. The minor "perturbations" observed closer to the leading edge of the particle cloud in Fig. 5b are presumably due to the initial random distribution of the

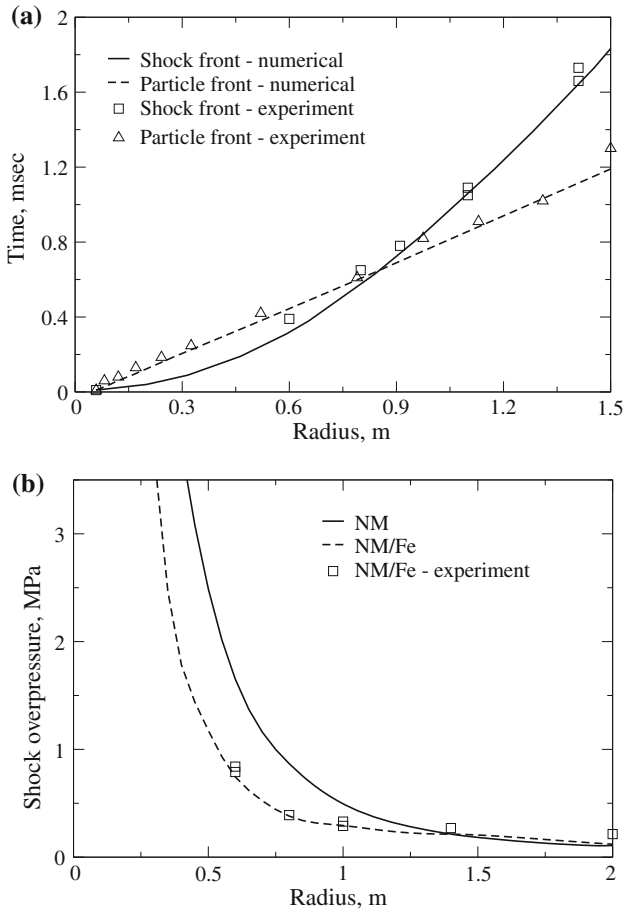

Fig. 4 Detonation of a 11.8 cm diameter Nitromethane charge with a dense loading of steel particles: **a** trajectory and **b** shock overpressure. The experimental data is obtained from [4]

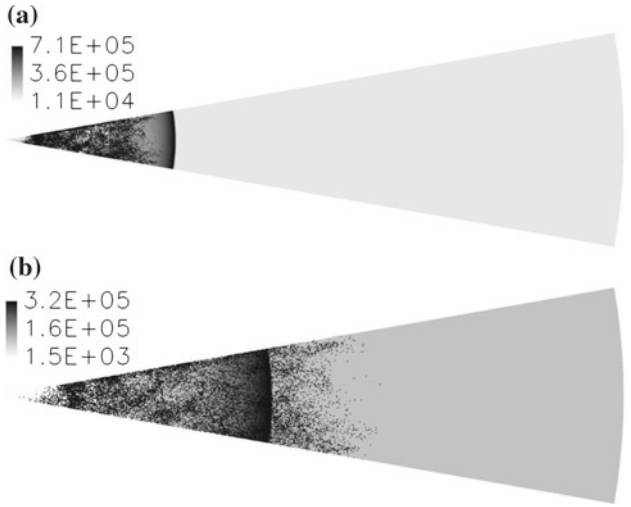

Fig. 5 Flow topography at **a** 0.38 ms and **b** 0.98 ms. The legend denotes the pressure field in Pa

particles. Moreover, post-detonation photography from [4] for the 463 μm particle size clearly indicates that the particle cloud for this heterogeneous explosive combination is nearly spherically-symmetric. For particles much smaller and lighter, the presence of particle jets and instabilities is a well-known feature of high-speed gas–particle mixtures; these phenomena will be investigated in the near future. In this study, we define the radius within which 98% of the particles are contained as the average particle cloud front.

When an explosive charge is detonated, a detonation wave propagates radially outwards within the charge. As this detonation wave reaches the charge surface, a blast wave propagates outwards and an expansion wave inwards. The outward moving blast wave decelerates and attenuates as it expands radially outwards. The inward moving expansion accelerates the flow outwards. In the heterogeneous case, this process is accompanied by inter-phase drag (viscous and pressure) effects, resulting in acceleration of the particle cloud outwards. During this process, the dense nature of the solid particle cloud creates inter-particle collisions/contact, resulting in further outward acceleration of the particles. This is due to the nature of the inter-particle forces trying to lower the bulk density of the packed solid particles within the explosive charge, which is accomplished only by a radially outward acceleration of the solid particles. After the particle front has propagated a distance of about 3–4 charge diameters, the volume fraction decreases to the dilute limit, and the inter-particle collision force becomes negligible. Furthermore, as the particles propagate outwards, the momentum transfer time scale increases due to three reasons: (1) decrease in the solid volume fraction results in a decrease of the drag coefficient; (2) decrease in the gas velocity results in a smaller velocity difference between the gas and the particles, and (3) decrease in the gas density. Due to inertia, the particles attain a terminal velocity, which remains nearly constant for a significant time, as observed by the near straight line trajectory of the particle front in Fig. 4a.

It is of interest to study the magnitude of the forces acting on the particles at early times, viz. the forces due to viscous drag (C_D), pressure drag (gas pressure gradient, $\frac{\partial p_g}{\partial x_i}$), and inter-particle collision/contact ($A_{c,i}$). To this end, in Fig. 6 we present the magnitude of the average acceleration/deceleration on all the particles due to these three forces. As evident, the average total acceleration on the particles is $\sim 5 \times 10^7$ m/s^2 at very early times ($\sim$0.01 ms), with that due to viscous and pressure drag being about 3–4 times that due to inter-particle collision/contact. Subsequently, the acceleration due to pressure drag decreases faster, as the gas pressure gradients decrease due to flow expansion. By $\sim$0.15 ms, the collision/contact forces become less significant in magnitude *vis-à-vis* the pressure drag, and both these forces are about one order of magnitude smaller than the viscous drag forces; beyond $\sim$0.175 ms, the collision/contact forces are

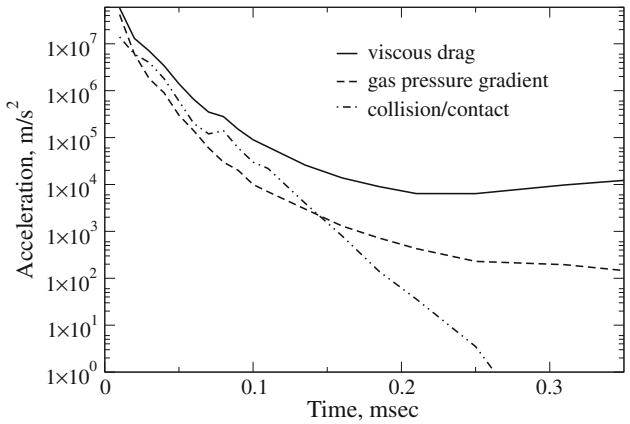

Fig. 6 Average acceleration/deceleration due to viscous drag, pressure drag (gas pressure gradient) and inter-particle collision/contact

two orders of magnitude smaller than the viscous drag; after ∼0.2 ms, the viscous drag forces emerge as the only significant force on the particles, with the acceleration/deceleration being about 10^4 m/s^2. Thus, although the collision/contact forces are significant only for the first ∼0.1 ms, these forces play a vital role in the initial distribution of particles, in particular near the leading edge of the expanding particle cloud where the collision/contact forces are more significant due to the higher solid volume fraction gradient.

The leading particles catch-up with the primary blast wave, as the latter has attenuated and slowed down owing to its spherical spreading. The particles at the front of the cloud overtake the primary blast wave and, subsequently, the momentum transfer time scale decreases slightly as the velocity difference between the particles and the gas is suddenly enhanced due to the ambient air being at rest. Thus, the particles that penetrate the blast wave are slowed down due to aerodynamic drag, allowing for the blast wave to again catch-up and overtake the solid particle front, as reported in [4]; however, our simulation domain is not radially long enough to capture this event. At the same time, the inward moving rarefaction over-expands the flow, giving rise to a secondary shock. This secondary shock is initially weak, and is swept outwards by the expanding detonation products and solid particles. During this initial outward passage, the strength of the secondary shock is augmented, as it propagates into regions of higher pressure. Subsequently, the secondary shock implodes inwards, as the pressure near the core has decreased considerably by the rarefaction wave. After its reflection from the origin, the secondary shock propagates outwards for the second time, and trails behind the primary shock. More physics on the formation and the propagation of the secondary shock is given in [36], albeit for a homogeneous charge. Our study shows that the primary and secondary shocks are slower for the heterogeneous charge when compared with the homogeneous charge containing the same amount of the high explosive by mass. Furthermore, the implosion of the secondary shock at the origin is delayed by about 0.6 ms for the heterogeneous charge due to the momentum and energy transfer to the particles.

3.2 Gas and particle momentum flux

It has been shown that the presence of particles results in impulse augmentation due to momentum transfer [6]. To demonstrate this phenomenon, the pressure and the momentum flux profiles at 0.9 and 1.55 m are compared for the homogeneous (NM) and heterogeneous (NM/Fe) charges containing the same amount of high explosive in Fig. 7. The pressure is lower for the NM/Fe charge when compared to NM (Fig. 7a). With the addition of solid particles, momentum and heat transfer from the detonation products to the solid particles results in a slower blast wave for the NM/Fe charge, and a corresponding lower pressure trace. The same argument holds for gas momentum flux profiles in Fig. 7b and c. It is observed that the solid momentum flux has a slightly higher peak than the gas momentum flux at the 0.9 and 1.55 m locations, contrary to the numerical predictions of [6]. This is owing to an increased distribution of solid particles closer to the leading edge of the particle cloud due to the gas pressure gradient term in the solid momentum equation. Furthermore, the solid momentum flux lasts for a longer time duration than the gas due to its inertia, as also reported in [6]. In the current EL approach, the absence of continuum modeling of the solid phase results in a "noisy" solid momentum flux profile.

In order to better understand the transfer of momentum from the gas to the particles, four different groups of particles are considered. 100 particles initially occupying radial locations between (0.058 ± 0.001) m are randomly chosen, and this group is named C58. Similar groups of 100 particles each are considered, initially occupying radial locations between (0.048 ± 0.001) m, (0.038 ± 0.001) m and (0.028 ± 0.001) m and named C48, C38 and C28, respectively. The average velocity of all the 100 solid particles belonging to each group, and the average local gas velocity as seen by each group are plotted in Fig. 8. It is seen that the terminal velocities can be arranged as C58 > C48 > C38 > C28, with the differences narrowing down between adjacent groups at smaller initial radial locations. This is due to an outer group being more free to move outwards than an inner one, the latter being constrained by the dense cloud of surrounding particles. The terminal velocity is reached within about 0.1 ms for all the groups, indicating the preponderance of the inter-particle interaction force, which is dominant at early times. Another reason for the rapid attainment of the terminal velocity is because the drag coefficient (and drag force) on the particles is higher in a denser cloud.

In Fig. 8, the diamond symbols indicate the times at which half the number of particles belonging to the corresponding

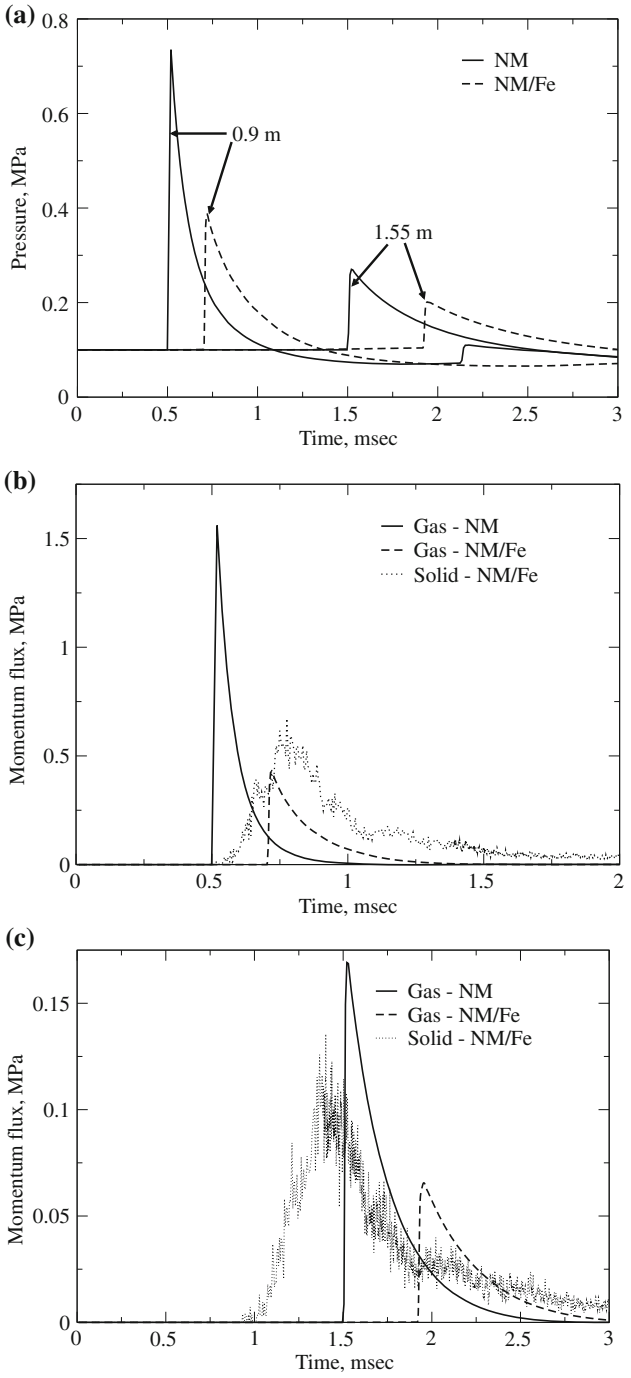

Fig. 7 Pressure (**a**) and momentum flux (**b**, **c**) profiles for NM and NM/Fe charges at 0.9 m (**a**, **b**) and 1.55 m (**a**, **c**)

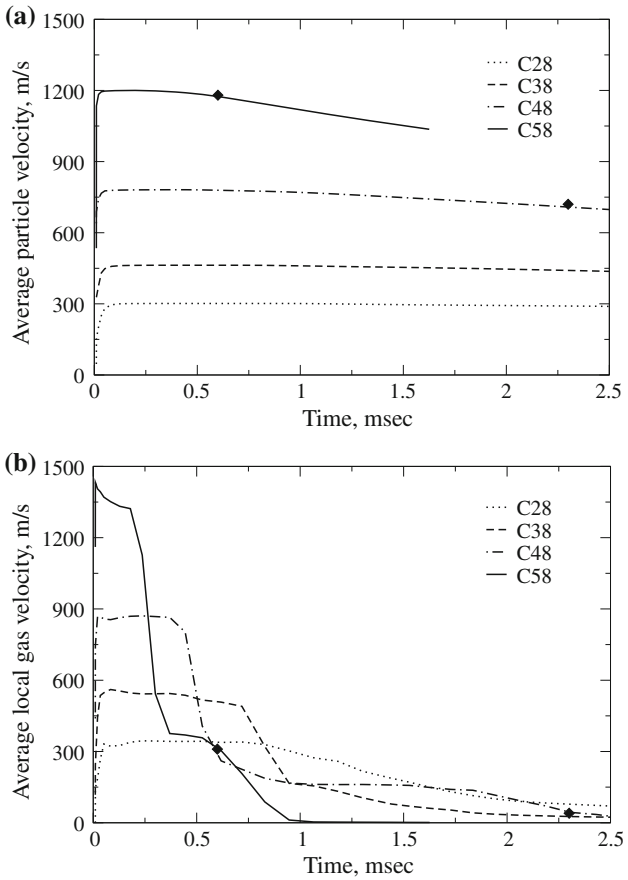

Fig. 8 Flow field behind the blast wave: **a** average particle velocity and **b** average local gas velocity for different groups of particles

group have penetrated the shock front. As evident from the figure, the average particle velocity of C58 and C48 groups start to decrease after penetrating the shock front. C38 and C28 are not observed to penetrate the shock front in the time duration of study. From the average local gas velocity seen by each group, it can be concluded that each group initially encounters different average local gas velocities in the order C58 > C48 > C38 > C28. Particles closer to the outer surface of the charge encounter higher local gas velocities due to the rapidly expanding gas, caused by the inward moving rarefaction wave. After an initial plateau, it is observed that the local gas velocities fall off, earlier (≈0.25 ms) for C58, but slightly later for the other groups, due to the faster travelling C58. For C58, C48 and C38, a second plateau is observed in the average local gas velocity as they approach the blast wave, but the two plateaus are coupled into one for C28. This second plateau lasts only for a short duration (≈0.25 ms) for C58, as the particles by virtue of being baster, catch-up with the leading blast wave earlier. For the chosen size of the simulation domain, the leading blast wave reaches the outer boundary before C38 and C28 groups, and thus, it could not be ascertained whether or not these inner groups penetrate the leading blast wave.

3.3 Impulsive loading

The total deliverable impulse from a heterogeneous charge can be estimated from the simulation data and typically, will be due to three components, i.e., pressure, gas and particle

momentum fluxes. These quantities can be integrated in time to obtain the total deliverable impulse. Some investigators [37,38] have considered the impulse due to excess gas pressure and particle momentum only, while others have considered the bending of a cantilever rod to quantify impulse [6]. Here, we consider the impulse deliverable to a "virtual wall" since the physical wall is not included in the current simulation. We define the total impulse (I) as:

$$I = \int_0^\infty \left(p_g - p_o\right)_{p_g > p_o} \mathrm{d}t + \int_0^\infty \frac{1}{2}\rho_g \alpha_g {u_g}^2 \mathrm{d}t + \int_0^\infty \frac{1}{2}\rho_p \alpha_p {u_p}^2 \mathrm{d}t, \tag{23}$$

where p_0 denotes the ambient pressure. The impulse due to pressure, gas and particle momentum fluxes are denoted as I_p, I_{gm} and I_{pm}, respectively. I_{pm} is computed as a summation over all the particles present in a small control volume around the radial distance of interest. The total impulse and its three components are shown in Fig. 9a, along with the ratio, I_{pm}/I_{gm}. The expansion of the gas and particle phases with radius causes the total impulse to decrease. I_{pm} is larger than I_{gm} at all radius, by a factor of about 3.5–4.75. Similar trends have been reported by other investigators [6]. In Fig. 9b, the impulse between the NM and NM/Fe charges containing the same amount of high explosive are compared at different radial locations along with the ratio of the impulses for NM/Fe and NM. As evident from the figure, impulse augmentation for the NM/Fe charge over the NM charge decreases from a factor of 2 in the near-field (∼4 charge dia.) to about 1.1 in the far-field (20 charge dia.). Thus, the advantage of adding solid particles to an explosive charge is more pronounced in the near-field, and asymptotes towards unity in the far-field. At farther distances from the charges, the significant slowing of the solid particles negates any impulse augmentations, thereby tending the behavior of a heterogeneous charge to that of a point source homogeneous charge.

The impulse estimate in Fig. 9 are the final impulsive loading delivered, i.e., obtained by integrating Eq. (23) up to a large time. It does not represent the transient behavior, i.e., whether the impulsive loading felt by an imaginary structure is sudden or gradual. To quantify this, the transient impulsive loading is presented at 0.5 and 2.25 m in Fig. 10, obtained by performing the integrations in Eq. (23) up to a certain time instant. The total impulse, as well as its individual components converge earlier at 0.5 m than at 2.25 m. At farther distances, the gas and particle phases are slower, and hence take a longer time to pass a given point, thereby resulting in a longer time duration for the impulse convergence. Since the blast wave arrives earlier than the particles at the 0.5 m location, only the impulse due to gas pressure and gas momentum

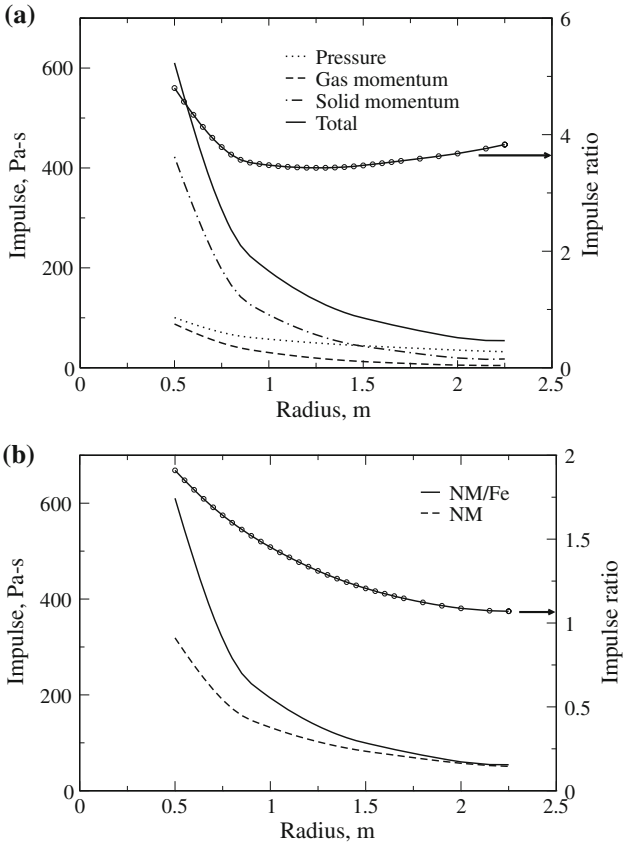

Fig. 9 Impulsive loading of a heterogeneous explosive: **a** total impulse and its components and **b** comparison between NM and NM/Fe charges. In **a**, the *line with the circles* represents the ratio between the solid and gas momentum impulses and corresponds to the right y-scale; in **b**, the *line with the circles* represents the ratio of the total impulses due to NM/Fe and NM and corresponds to the right y-scale

contribute initially; subsequently, after the particles arrive, their contribution takes over as the dominant component. At this location, the passage of the primary blast wave raises the pressure, but subsequently falls to sub-atmospheric levels and low gas velocities, and thus all the pressure and gas momentum impulse are delivered in a very short time (within ∼0.6 ms). On the other hand, the intermediate velocity particles take a longer time to pass the 0.5 m location, and thus the impulse due to solid momentum converges later (∼2 ms).

At the 2.25 m location, the reverse is observed for the early contribution to the total impulse. Since the particles reach this location earlier than the blast wave, they are the dominant early contributors; beyond about 3.5 ms, with the arrival of the blast wave, the pressure impulse takes over as the dominant contributor. Also at this location, the convergence of the impulse due to pressure and gas momentum occur almost at the same time (∼4.75 ms), but that due to the particles is delayed until ∼7 ms. Due to the shifts of the solid and gas phases as the primary contributor, the transient total impulse at the 2.25 m location occurs in two phases,

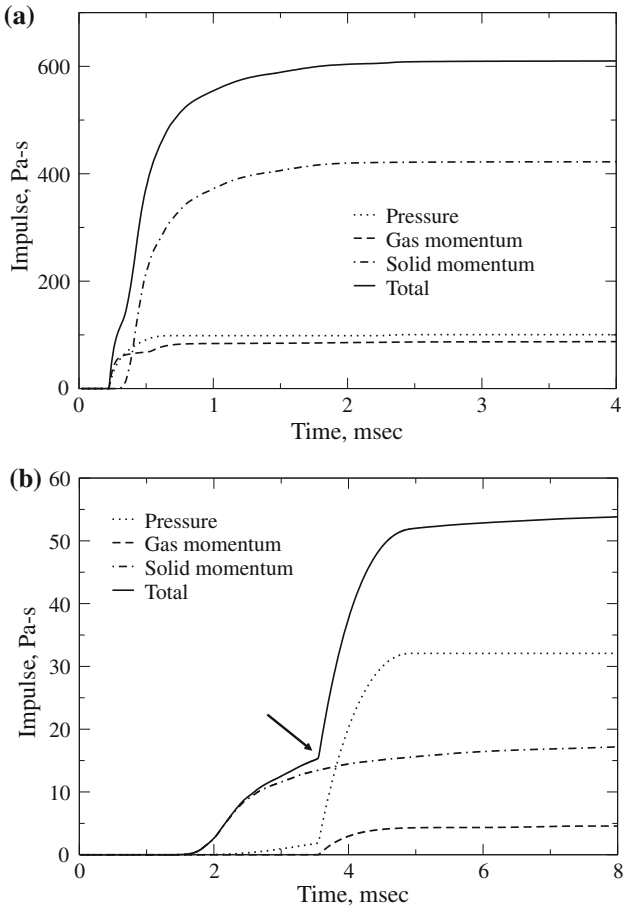

Fig. 10 Transient impulse and its components for a heterogeneous explosive at radial locations: **a** 0.5 m and **b** 2.25 m

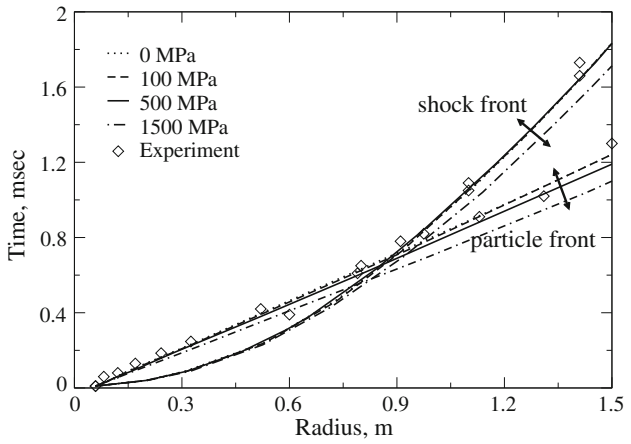

Fig. 11 Effect of collision model: shock and particle front trajectories for different collision/contact model coefficients (P_s) (the results for the 0 MPa case are nearly coincident with the 100 MPa case, and thus the former are not clearly visible)

resulting in a sudden slope change observed in the total impulse, indicated by the arrow in Fig. 10b. Thus, while an imaginary structure at the 0.5 m location may destruct/deform gradually, its response will occur in two phases at the 2.25 m location. While most civil engineering structures may have a slow response, solid propellants/explosives have faster responses to the impulsive loading [39]. For instance, if the heterogeneous explosive charge under study is used as an igniter of a larger solid propellant/explosive, the transient nature of the impulse can be very critical in its ignition. Here, ignition is achieved by a combination of mechanical and thermal stresses. For these studies, transient impulsive response can be very critical in the ignition event.

3.4 Sensitivity to collision model coefficient

For the heterogeneous blast wave simulations performed hitherto, the collision model coefficient, P_s was chosen as 500 MPa, based on an order of magnitude analysis of the drag and collision/contact forces on a particle. In order to better elucidate the sensitivity of the results to the collision model coefficient, four other studies are carried out: (1) $P_s = 0$ MPa, (2) $P_s = 100$ MPa, (3) $P_s = 250$ MPa and (4) $P_s = 1500$ MPa. Figure 11 shows the primary blast wave and the particle front trajectories for different values of P_s so chosen, along with $P_s = 500$ MPa used hitherto. The blast wave trajectory is nearly unaffected by the choice of the collision/contact model coefficient, P_s for values in the range 0–500 MPa. For P_s in the same range (0–500 MPa), the particle front trajectory is observed to be only slightly faster for the higher collision model coefficient, albeit not to a significant extent.

From Fig. 11, for $P_s = 1500$ MPa, both the blast wave and particle front trajectories are significantly faster. A value of $P_s = 1500$ MPa is unphysically high and causes the particles to travel much faster, as well as more concentrated towards the leading edge of the cloud, due to the associated higher collision/contact forces at early times (0–0.1 ms). Furthermore, $P_s = 1500$ MPa results in inter-granular stresses larger than the ultimate strength of steel, resulting in the rupture of the particles, unaccounted for in this study. Since the particle cloud is initially lagging behind, the blast wave trajectory for the case with $P_s = 1500$ MPa matches with the other cases until about 0.6 ms, as the particles have no influence on the blast wave until this time. However, beyond 0.6 ms, as the leading particles get closer to the blast wave, they compress the gas, which decreases the decay rate of the primary blast wave. Due to the unphysically high particle speeds and concentration, this compression effect is strong for the case with $P_s = 1500$ MPa. Indeed, we observe a second compression wave (not to be confused with the secondary shock) in front of the particle cloud as they catch-up with the blast wave, not shown here for brevity. The presence of this compression wave is more pronounced for $P_s = 1500$ MPa than for the

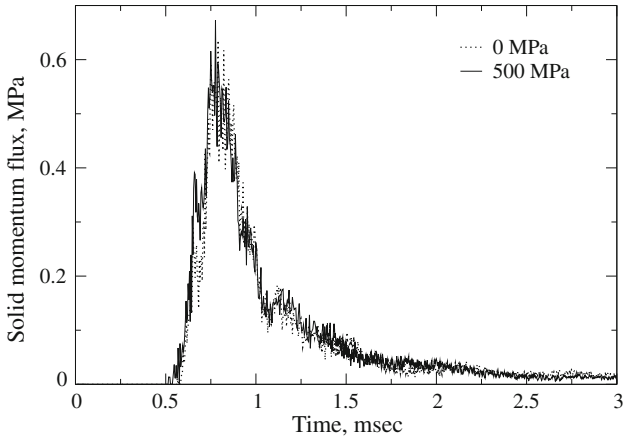

Fig. 12 Effect of collision model on the solid momentum flux

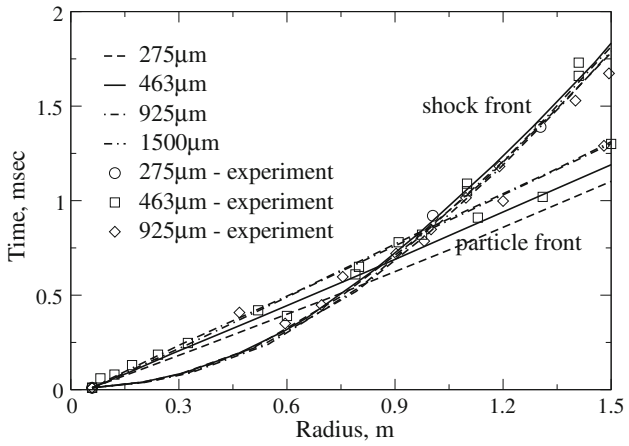

Fig. 13 Effect of particle size on the primary blast wave and particle front trajectories. Experimental data is from [4]; experimental particle front for the 275 μm size not available in [4]

other lower values considered due to the unphysically high speeds and higher leading concentration of the particle cloud.

High values of the collision model coefficient (P_s) not only cause higher particle speeds, but higher particle concentration near the outer boundary of the particle cloud. At early times (0–0.1 ms), the ensuing particle collisions tend to force the particles outward in the radial direction. That is to say, near the center of the charge, inter-particle collisions are equally likely in all directions; but for particles near the cloud boundary, collisions are biased and tend to force the particles outwards. Subsequently, as the particles reach farther radial distances, the solid volume fraction approaches the dilute limit, and the collision/contact force becomes negligible. However, since a few more particles are concentrated closer to the outer boundary of the cloud at early times, this distribution of particles is maintained even long after the collision/contact force becomes negligible.

To understand the effect of the initial solid particle collisions, the solid momentum flux profile is shown in Fig. 12 at the 0.9 radial location for $P_s = 0$ and 500 MPa. For both cases, although the solid momentum flux begins to rise around 0.6 ms at the 0.9 m location, the peak is marginally higher when $P_s = 500$ MPa due to a greater particle concentration near the cloud's outer edge. Due to this, the total impulse is about 6% higher for $P_s = 500$ MPa than with $P_s = 0$ MPa, primarily due to more particles accumulated closer to the leading edge of the particle cloud (not shown here for brevity).

3.5 Effect of particle size

The baseline numerical solution for this study is computed for steel particles 463 μm in diameter in a 11.8 cm diameter charge corresponding to a particle volume fraction of 62%. To better understand the effect of particle size on the impulse characteristics of heterogeneous explosive charges, we consider steel particles with diameters 50, 100, 275, 925 and 1500 μm, for the same charge diameter and initial particle volume fraction, and compare the results with those for the baseline charge. Figure 13 shows the shock and particle front trajectories for a range of the selected particle diameters. As observed, the shock front is unaffected by the solid particle size, but the particle front is observed to be slightly faster for smaller particles. For instance, the trajectory of the leading edge for the 275 μm particles is observed to be 100–150 m/s faster than that for 925 μm particles, correlating to a distance of 0.1–0.15 m over a time frame of 1 ms or about one charge diameter distance. Although the authors of [4] concluded that the particle front trajectory is insensitive to the particle size beyond 275 μm, based on our numerical results, we believe that the differences, although small, are distinctive enough to conclude that smaller particles travel faster than larger particles. At a radial distance of 12 charge diameters, smaller particles will propagate about one charge diameter farther.

Figure 14 shows the solid momentum flux profiles at the 0.9 m radial location for charges containing 463 and 925 μm particle sizes. Since the 463 μm particles are slightly faster than the 925 μm particles, the solid momentum flux starts to rise earlier for the former. However, the peak solid momentum flux is ∼15% higher for the 925 μm particles, as these are slower and hence, slightly more concentrated in space. Nevertheless, the impulse due to solid momentum is nearly identical for the two particle sizes. Thus, larger particles are characterized by a higher peak momentum flux of shorter duration than for smaller particles, yet both provide nearly the same contribution to the total impulse.

The total impulse for charges with different particle sizes in the range 50–1500 μm are shown in Fig. 15a. Particle sizes above 275 μm are observed to result in the same total impulse, thus indicating insensitivity of the total impulse

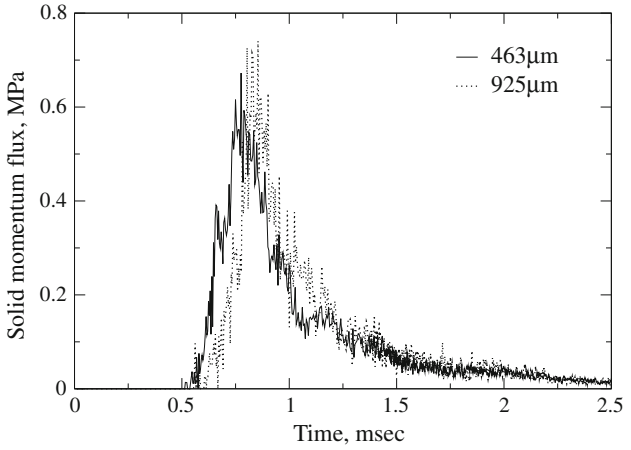

Fig. 14 Effect of particle size on the solid momentum flux profiles at 0.9 m

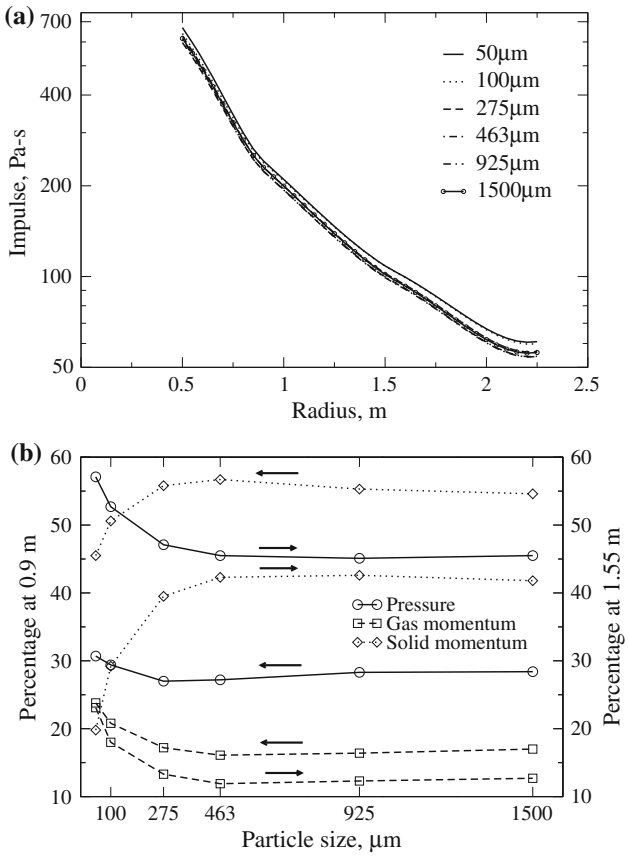

Fig. 15 Effect of particle size: **a** total impulse; **b** components of total impulse expressed as a percentage of the total. The *arrows* in **b** denote the left or right y-scale to which each curve corresponds to

to particle size beyond 275 μm. This emphasizes that the total impulse is directly related to the total mass of metal in the charge for charges with particle sizes in the range 275–1500 μm. For the 50 and 100 μm size, the total impulse is ∼8% higher than the larger particle sizes, as these small particles pick up significant amounts of momentum from the gas, and are more concentrated closer to the leading edge of the exploding particle cloud. After these smaller particles penetrate the leading blast wave, they surrender most of their momentum back to the gas, as they have lesser inertia compared to the larger particles; however, by virtue of being more concentrated closer to the leading edge of the particle cloud, the total impulse is still superior for the 50 and 100 μm particles.

In Fig. 15b, the three components of the total impulse, i.e., due to pressure, gas momentum and solid momentum, as percentage of the total impulse are shown at the 0.9 and 1.55 m locations. The percentage of the pressure impulse is observed to increase for all particle sizes from 0.9 to 1.55 m, while the percentage of the gas and solid momentum are observed to decrease between these two radial locations. As the gas expands out farther, it slows down, and thus contributes less from its momentum to the total impulse. As the solid particle cloud expands radially outwards, its concentration decreases as it disperses into more free space, and thus also contributes less from its momentum at farther distances. The pressure impulse is ∼28% of the total impulse for particle sizes larger than 275 μm at the 0.9 m location, and decreases at the 1.55 m location from 57% for 50 μm to 45% for 1500 μm particles. Furthermore, the solid momentum flux contribution increases with particle size at both locations, i.e., from 45 to 55% at 0.9 m, and from 20 to 42% at 1.55 m, as we increase the particle size from 50 to 1500 μm. Owing to a higher inertia, larger particles contribute more to the total impulse from solid momentum than their smaller counterparts. Due to this reason, the contribution from gas momentum flux decreases at both locations with increasing particle size. Furthermore, it is interesting to note the rapid changes in the individual contributions of the different impulse components below the 275 μm particle size due to the significant slowing of these smaller particles at farther distances.

3.6 Effect of initial volume fraction

In this section, we study the effect of the initial volume fraction in the explosive charge. When fewer solid particles occupy the same size charge, more volume is available to the high explosive, and hence higher is the explosive mass (and detonation energy). Thus, with a decreased initial solid volume fraction, more explosive energy is available to drive fewer solid particles. To illustrate the dependence of the initial solid volume fraction, we consider the 11.8 cm dia. charge with 463 μm dia. steel particles, the same collision model coefficient $P_s = 500$ MPa, but with an initial solid volume fraction $\alpha_{p,\text{initial}} = 0.3$, and compare it with the baseline $\alpha_{p,\text{initial}} = 0.62$ charge. The trajectories of the leading blast wave and the particle front for these two charges are shown in Fig. 16a, along with the experimental data

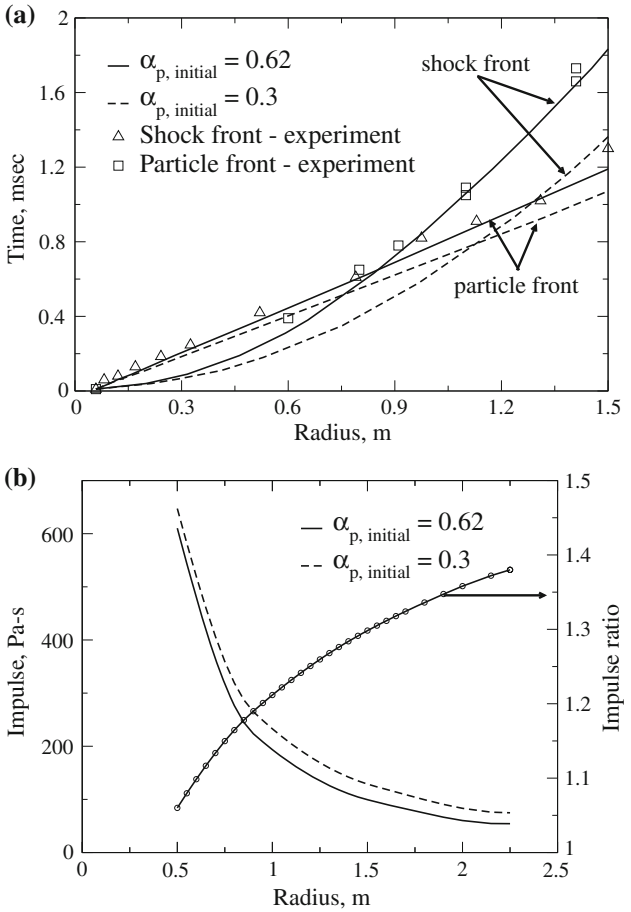

Fig. 16 Effect of initial volume fraction: **a** blast wave and particle front trajectories; **b** total impulse. In **b**, the *line with the circles* represents the ratio of the total impulses due to $\alpha_{p,\text{initial}} = 0.3$ and $\alpha_{p,\text{initial}} = 0.62$, and corresponds to the right y-axis

for $\alpha_{p,\text{initial}} = 0.62$ from [4]. As evident, the leading blast wave and the particle front are significantly faster for the decreased initial solid volume fraction $\alpha_{p,\text{initial}} = 0.3$, due to the higher explosive energy available to drive fewer solid particles. However, the distance required for the particle front to overtake the leading blast wave is higher by ∼30% for $\alpha_{p,\text{initial}} = 0.3$, contrary to the numerical predictions of [4]. We attribute these differences to the different initial conditions used in the current paper; furthermore, experimental data for $\alpha_{p,\text{initial}} = 0.3$ is not available in literature, and thus the overtaking distance is not verifiable for the decreased initial solid volume fraction.

Our study also shows that the peak pressure and gas momentum flux profiles at a radial location are higher for $\alpha_{p,\text{initial}} = 0.3$ *vis-à-vis* $\alpha_{p,\text{initial}} = 0.62$, as more explosive mass is available for the former; however, the peak solid momentum flux at a radial location is higher for the latter, as more particles are available for the same (these results are not presented here for brevity). Since this investigation is primarily focused on impulsive loading aspects of heterogeneous explosives, we present the total impulses of the two said initial volume fraction charges in Fig. 16b, along with their ratio. As evident, the total impulse is only 6% higher at the 0.5 m radial location for $\alpha_{p,\text{initial}} = 0.3$, but is 38% higher for the same charge at the 2.25 m radial location. This suggests that in the near-field, the impulse augmentation by adding more solid particles to the charge can be easily compensated by otherwise having more high explosive. However, in the far-field, significant impulse augmentation is achieved by substituting part of the solid volume in the charge with the high explosive, as this excess gas phase energy enhances the far-field impulsive loading. In the future, we will also investigate whether these conclusions hold for other choices of the metal in the initial charge, as well as other choices of the high explosive.

4 Conclusions

Simulation of flow and particle motion associated with the interaction of a blast wave with non-reacting particles in a heterogeneous explosive charge has been investigated by means of a three-dimensional simulation. This is achieved with the use of a new Eulerian–Lagrangian two-phase model capable of capturing the initial dense flow-field and the interactions of particles with shock and the gas phase. Several validation studies have been carried out to establish the accuracy of the hydrocode to emphasize the efficacy of the solver. The pressure, velocity and momentum flux distributions are used to estimate the total impulse at different radial locations. The heterogeneous charge is found to deliver an impulse of about two times a homogeneous charge containing the same amount of high explosive in the near-field (∼4 charge dia.), but only slightly more in the far-field (∼20 charge dia.).

At intermediate distances (∼4 charge dia.) from the initial charge, the gas and particles contribute simultaneously to the total impulse, due to which the transient impulse rises gradually. At farther distances (∼20 charge dia.), the particles provide the only initial contribution, and that of the gas is delayed, due to which the transient impulse occurs in two phases. This result has implications for the dynamic response of structures subjected to the blast created by the detonation of this type of charges. The particle collision/contact model does not seem to have a significant effect on particle trajectories at low to intermediate ranges, except for a case where the collision model coefficient has been set to an excessively high value. With a higher collision model coefficient (P_s), slightly more particles are concentrated towards the leading edge of the particle cloud, resulting in a higher peak solid momentum flux, and consequently a higher impulse (∼6%).

The primary shock front is not affected by the particle size, but some slight differences exist for the particle trajectory. For particle size range 275–1500 μm, smaller particles travel

slightly faster, albeit only to an extent of about a charge diameter farther distance travelled at a radial location of about 12 charge diameters. For charges containing the same mass of high explosive and metal, the total impulsive loading is insensitive to the particle size for particle sizes beyond 275 μm; however, the individual impulse components are sensitive. Larger particles deliver a higher peak solid momentum flux, albeit for a shorter time. While the pressure impulse percentage increases at greater distances, the gas and particle momentum impulse percentages decrease. This result is true for all of the particle sizes addressed in this study.

The present work has demonstrated a robust simulation model that can be used to study the multiphase blast wave created by the detonation of a condensed explosive material loaded with a large mass of metal particles. Future studies will focus on more detailed evaluation of the sensitivity of the post detonation structure on the explosive initial charge configuration, including the properties of the particles. Studies to better understand the dependence of the impulsive loading to the choice of the metal, initial volume fraction, and the presence of reactive particles will be addressed in the near future.

Acknowledgments This research was supported by the Office of Naval Research, the Air Force Office of Scientific Research, and the Munitions Directorate, Air Force Research Laboratory. Simulations were performed at the Naval Oceanographic Office and U.S. Army Research Laboratory Major Shared Resource Center. The first author also acknowledges the private discussions with Dr. Richard Saurel of Polytech Marseille, France, on the development of the DEM. Dr. Franklin Genin of the Georgia Institute of Technology provided some valuable comments.

Appendix A

For the solution of the half-Riemann problem at the multiphase contact, two unknowns, viz. p^* and ρ^* are to be solved using the appropriate two relations for a compression or a rarefaction, as the case may be.

Compression

For a compression, the equations are obtained from Toro [40]. Consider the case of a right traveling shock wave and an incompressible solid on the left. Let subscript 'r' correspond to the right state and superscript '*' the interface. The steady shock relations for a right travelling shock give

$$M_r{}^2 = \frac{\rho_{g,r}\left(p^* - p_{g,r}\right) D_r}{D_r - 1}, \tag{A-1}$$

where M_r is defined as

$$M_r = \frac{p^* - p_{g,r}}{u^* - u_{g,r}} \tag{A-2}$$

and D_r is the density ratio $\rho^*/\rho_{g,r}$ across the shock. The Rankine–Hugoniot relation is given by

$$e^* - e_{g,r} = \frac{1}{2}\left(\frac{p_{g,r}}{\rho_{g,r}}\right)\frac{(H_r + 1)(D_r - 1)}{D_r}, \tag{A-3}$$

where H_r is the pressure ratio $p^*/p_{g,r}$ across the shock. Using the equation of state for the '*' and 'r' states, the variables e^* and $e_{g,r}$ in the above equation can be replaced by a function of the corresponding state pressure and density. This gives rise to two equations in two variables (p^* and ρ^*), which are solved numerically. Similar expressions can be obtained for a left travelling shock wave with the incompressible solid on the right.

Rarefaction

For a rarefaction, the isentropic relation and Riemann invariant are applied across the '*' and left or right gas state, as the case may be. The isentropic relation applicable for the JWL equation of state is given by [19] as follows

$$p_g = A\exp\left(\frac{-R_1\rho_o}{\rho_g}\right) + B\exp\left(\frac{-R_2\rho_o}{\rho_g}\right) + C\left(\frac{\rho_o}{\rho_g}\right)^{-(1+\omega)}. \tag{A-4}$$

The Riemann invariant for a left moving rarefaction, applicable for a generic equation of state is given by

$$u_g + \int \frac{a_g}{\rho_g}\mathrm{d}\rho_g = \text{constant}, \tag{A-5}$$

where a_g denotes the speed of sound in the gas. For a right moving rarefaction, the '+' is replaced by '−'. The above two equations are applied for the '*' and left or right state, as the case may be, thus giving rise to two equations in two unknowns (p^* and ρ^*). These are numerically solved to obtain p^* and ρ^*.

For a perfect gas, the above equations simplify to close-form expressions for p^* and ρ^*, thus simplifying their numerical implementation.

Appendix B

Particle dispersion in a shock tube

Particle dispersion due to passage of a shock wave is a canonical test case to establish the ability of the solver to capture particle motion and dispersion (which requires proper drag modeling) during shock-particle interaction. The dispersion of a nylon particle ($\rho_p = 1170$ kg/m^3) 2 mm dia. subjected to a Mach 1.56 shock is investigated repeating an earlier experimental and numerical study by Devals et al. [41], who concluded that the particle trajectory and the velocity agree

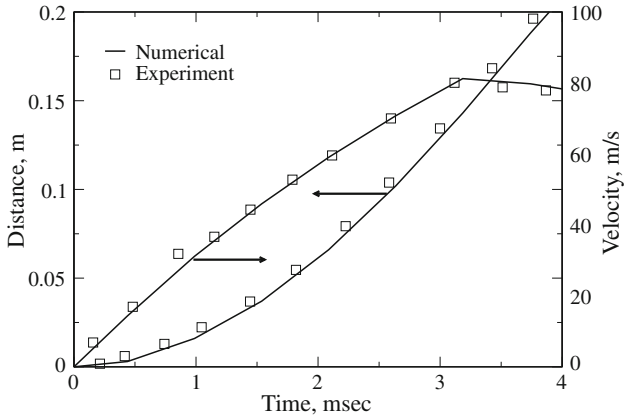

Fig. 17 Evolution of particle trajectory (*left axis*) and velocity (*right axis*) with time. The experimental data is from [41]

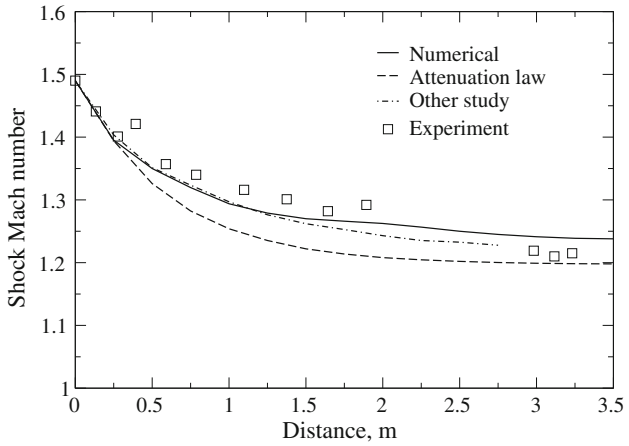

Fig. 18 Planar shock wave attenuation in dust-gas suspension. The experimental data is from [44]; the attenuation law is from [45]; the other study is from [46]

with the drag law of Igra and Takayama [42]. Initialization is based on a high pressure region, released at zero time and allowed to expand. A domain of 3.75 m in the axial direction and a cross-section of 8 cm × 8 cm is discretized using a grid of size 375 × 8 × 8. No flux boundary conditions are used on the shock tube walls. The particle trajectory and the velocity evolution with time are shown in Fig. 17. The present study agrees well with the measured data and is consistent with other model predictions of similar test cases. Since this shock tube does not have an outlet, the shock reflects from the end wall, which causes the particle velocity to level off at later times (>3 ms), and the particle trajectory to follow a near-straight line at later times.

Shock propagation through dust-gas suspension

The attenuation of a shock wave upon its passage through a dilute gas–particle mixture is also studied using a drag law applicable for this regime [43]. This is a well established test case studied earlier using both experiments and numerical modeling [44]. A shock wave of a prescribed Mach number, $M_s = 1.49$ passes through a cloud of glass particles (27 μm dia, $\rho_p = 2500$ kg/m^3) initially occupying a mass loading ratio, $\eta = 0.63$. The same shock tube geometry [44] is simulated using a no-flux boundary condition in the shock tube walls, and supersonic outflow at the exit plane of the low pressure region. Initialization is achieved by means of a high pressure region that is then allowed to expand. Although the experiments were performed in a circular cross-section shock tube [44], we used a square cross-section, which should not affect the results due to the one-dimensionality of the problem. A shock tube 7.81 m long is considered, with a cross section being a square of side 5 cm, and is resolved using a 781 × 10 × 10 grid. Figure 18 shows the shock wave Mach number as it propagates through the gas–particle mixture. Also shown are the attenuation rates obtained by Aizik et al. [45], and numerical results obtained by other investigators [46]. The shock wave attenuation predicted by the present hydrocode is in good agreement with other studies.

Shock propagation through dense gas–particle mixture

In order to validate the Eulerian–Lagrangian DEM approach implemented in the code, the problem of shock wave propagation through a dense gas–particle mixture is investigated and compared to available experimental data [47]. The propagation of a Mach 1.3 shock into a cloud of glass particles 1.5 mm dia., and occupying 65% volume of a 2 cm thick bed is considered using the drag law of Crowe et al. [25]. The same shock tube geometry [47] is used with no-flux boundary conditions along the side walls, and supersonic outflow in the far extreme of the low pressure region. As before, the initialization is based on a high pressure region to generate the shock wave. The shock tube is 6 m long, with a cross-section of 13 cm × 13 cm, and this is simulated using a 600 × 13 × 13 grid. The upstream and downstream pressure traces are presented in Fig. 19, and the simulation results are in good agreement. Also shown are the results obtained with the DEM turned off, i.e., the simulation carried out without any dense effects accounted (note that this is not physical as the volume occupied by the solid particles is not blocked for the gas). As expected, with the DEM off, the upstream pressure is under-predicted and the downstream over-predicted, as without the blockage due to the solid particles, more of the shock energy is transmitted downstream and less upstream; also for the same reason, the transmitted shock arrives at the downstream location about 0.4 ms earlier with the DEM turned off. This study validates the DEM methodology and demonstrates the blockage effects in gas–particle flows.

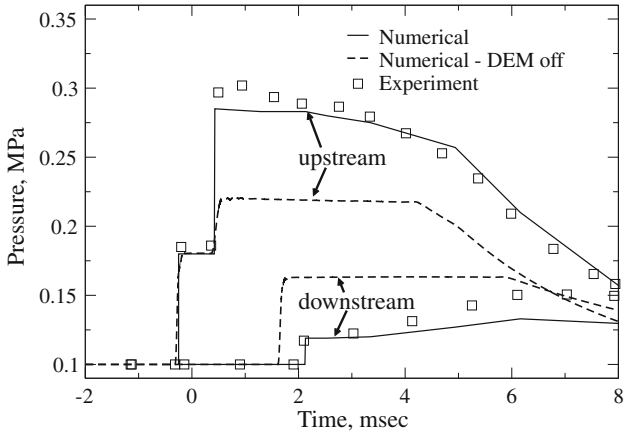

Fig. 19 Pressure traces upstream and downstream of a dense particle bed subjected to a shock wave. The experimental data is from [47]

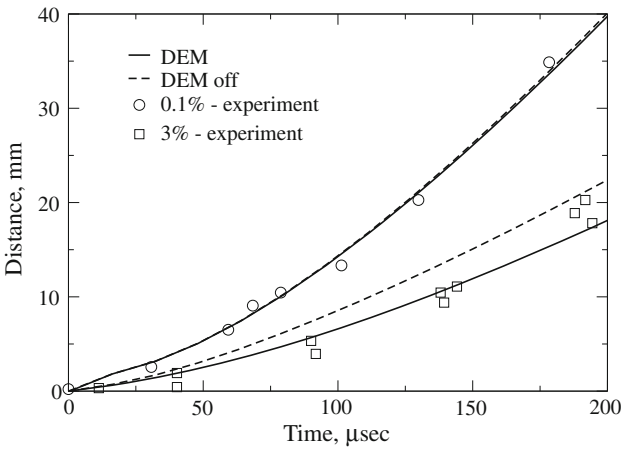

Fig. 20 Dispersion of acrylic plastic clouds of initial volume fractions (i) 0.1% and (ii) 3% by a Mach 2.8 shock. The experimental data is from [48]

Shock-induced dispersion of acrylic plastic clouds

To illustrate the significance of the just mentioned blockage effect and the concomitant available shock energy upstream and downstream of the particle cloud, we next consider the problem of the dispersion of a cloud of acrylic plastic cloud due to a Mach 2.8 shock wave in air. Experimental data for this configuration can be obtained from [48], for acrylic plastic clouds containing 300 µm dia. particles, with initial volume fractions (i) 0.1% and (ii) 3%, performed in a 6.5 m long shock tube with a 52 mm × 52 mm cross section. We simulate the problem with a 1250 × 10 × 10 grid using Rankine–Hugoniot conditions to initialize the flow behind the initial Mach 2.8 shock, and consider the two different aforesaid volume fractions for the initial acrylic plastic particle cloud. We use the drag law from the numerical study also performed in [48]. The trajectory of the left boundary of the cloud as it disperses after interacting with the shock is shown in Fig. 20; simulations are performed with the DEM as well as turning off DEM. As evident, for a 0.1% initial solid volume fraction, the dense approach is not essential as the trends agree with experimental data, both with and without DEM; on the other hand, for a 3% initial volume fraction, the dispersion characteristics match better with experimental data with the DEM. As seen in the previous test study, with the DEM off, since accurate blockage to the flow of gas by the particle cloud is not accounted for, the transmitted shock and the flow behind it are stronger, thereby the dispersion is faster in relation to the physical case with DEM, i.e., with the blockage accounted for. From this study we conclude that, whereas 0.1% can be treated dilute for simulations, 3% initial volume loading requires the use of a two-phase methodology. We note that although 3% may seem low in terms of volume fraction, the passage of the shock compresses the particle cloud resulting in solid volume fractions as high as 10%, thereby necessitating the use of the dense approach.

Another observation from Fig. 20 is that the dispersion is more prominant for the 0.1% volume fraction cloud, as this results in lesser blockage and therefore a stronger transmitted gas flow.

References

1. Lee, J.J., Brouillette, M., Frost, D.L., Lee, J.H.S.: Effect of diethylenetriamine sensitization on detonation of nitromethane in porous media. Comb. Flame **100**, 292–300 (1995)
2. Lanovets, V.S., Levich, V.A., Rogov, N.K., Tunik, Y.V., Shamshev, K.N.: Dispersion of the detonation products of a condensed explosive with solid inclusions. Comb. Expl. Shock Waves **29**(5), 638–641 (1993)
3. Milne, A.M.: Detonation in heterogeneous mixtures of liquids and particles. Shock Waves **10**, 351–362 (2000)
4. Zhang, F., Frost, F.D., Thibault, P.A., Murray, S.B.: Explosive dispersal of solid particles. Shock Waves **10**, 431–443 (2001)
5. Zhang, F., Thibault, P.A., Link, R.: Shock interaction with solid particles in condensed matter and related momentum transfer. Proc. Math. Phys. Eng. Sci. **459**(2031), 705–726 (2003)
6. Frost, D.L., Ornthanalai, C., Zarei, Z., Tanguay, V., Zhang, F.: Particle momentum effects from the detonation of heterogeneous explosives. J. Appl. Phys. **101**, 113529 (2007)
7. Massoni, J., Saurel, R., Lefrancois, A., Baudin, G.: Modeling spherical explosions with aluminized energetic materials. Shock Waves **16**, 75–92 (2006)
8. Ripley, R., Zhang, F., Lien, F.S.: Detonation interaction with metal particles in explosives. In: Proceedings of the 13th International Detonation Symposium, July 23–28, Norfolk, Virginia, USA (2006)
9. Balakrishnan, K., Genin, F., Nance, D.V., Menon, S.: Numerical study of blast characteristics from detonation of homogeneous explosives. Shock Waves (2009). doi:10.1007/s00193-009-0236-4
10. Balakrishnan, K., Menon, S.: On the role of ambient reactive particles in the mixing and afterburn behind explosive blast waves. Combust. Sci. Technol. **182**(2), 186–214 (2010)
11. Baer, M.R., Nunziato, J.W.: A two-phase mixture theory for the Deflagration-to-Detonation-Transition (DDT) in reactive granular materials. Int. J. Multiphase Flow **12**(6), 861–889 (1986)

12. Kapila, A.K., Menikoff, R., Bdzil, J.B., Son, S.F., Stewart, D.S.: Two-phase modeling of deflagration-to-detonation transition in granular materials: reduced equations. Phys. Fluids **13**(10), 3002–3024 (2001)
13. Abgrall, R., Saurel, R.: Discrete equations for physical and numerical compressible multiphase mixtures. J. Comput. Phys. **186**, 361–396 (2003)
14. Chinnayya, A., Daniel, E., Saurel, R.: Modelling detonation waves in heterogeneous energetic materials. J. Comput. Phys. **196**, 490–538 (2004)
15. Le Metayer, O., Massoni, J., Saurel, R.: Modelling evaporation fronts with reactive Riemann solvers. J. Comput. Phys. **205**, 567–610 (2005)
16. Chang, C.H., Liou, M.S.: A conservative compressible multifluid model for multiphase flow: shock-interface interaction problems. AIAA paper 2005-5344 (2005)
17. Chang, C.H., Liou, M.S.: A robust and accurate approach to computing compressible multiphase flow: stratified flow model and $AUSM^+$-up scheme. J. Comput. Phys. **225**, 840–873 (2007)
18. Cowperthwaite, M.: Significance of some equations of state obtained from shock-wave data. Am. J. Phys. **34**(11), 1025–1030 (1966)
19. Zukas, J.A., Walters, W.P.: Explosive Effects and Applications. Springer, Berlin (1998)
20. Toro, E.F.: Riemann Solvers and Numerical Methods for Fluid Dynamics. Springer, Berlin (1999)
21. Batten, P., Clarke, N., Lambert, C., Causon, D.M.: On the choice of wavespeeds for the HLLC Riemann solver. SIAM J. Sci. Comput. **18**(6), 1553–1570 (1997)
22. Liska, R., Wendroff, B.: Comparison of several difference schemes on 1D and 2D test problems for the Euler equations. SIAM J. Sci. Comput. **25**(3), 995–1017 (2003)
23. Patankar, N.A., Joseph, D.D.: Modeling and numerical simulation of particulate flows by the Eulerian–Lagrangian approach. Int. J. Multiphase Flow **27**, 1659–1684 (2001)
24. Snider, D.M.: An incompressible three-dimensional multiphase particle-in-cell model for dense particle flows. J. Comput. Phys. **170**, 523–549 (2001)
25. Crowe, C., Sommerfeld, M., Tsuji, Y.: Multiphase Flows with Droplets and Particles. CRC Press, Boca Raton (1998)
26. Gonthier, K.A., Powers, J.M.: A high-resolution numerical method for a two-phase model of deflagration-to-detonation transition. J. Comput. Phys. **163**, 376–433 (2000)
27. Akhatov, I.Sh., Vainshtein, P.B.: Transition of porous explosive combustion into detonation. Combust. Expl. Shock Waves **20**(1), 63–69 (1984)
28. Michaelides, E.E., Feng, Z.: Heat transfer from a rigid sphere in a nonuniform flow and temperature field. Int. J. Heat Mass Transf. **37**(14), 2069–2076 (1994)
29. Saurel, R.: Private communication (2007)
30. Munkejord, S.T., Papin, M.: The effect of interfacial pressure in the discrete-equation multiphase model. Comput. Fluids **36**, 742–757 (2007)
31. Xu, S., Aslam, T., Stewart, D.S.: High resolution numerical simulation of ideal and non-ideal compressible reacting flows with embedded internal boundaries. Combust. Theory Model. **1**, 113–142 (1997)
32. Xu, S., Stewart, D.S.: Deflagration-to-detonation transition in porous energetic materials: a comparative model study. J. Eng. Math. **31**, 143–172 (1997)
33. Bdzil, J.B., Stewart, D.S., Jackson, T.L.: Program burn algorithms based on detonation shock dynamics: discrete approximations of detonation flows with discontinuous front models. J. Comput. Phys. **174**, 870–902 (2001)
34. Genin, F., Menon, S.: Dynamics of sonic jet injection into supersonic crossflow. J. Turbulence (2009, to appear)
35. Oliver, E.C., Daymond, M.R., Withers, P.J.: Interphase and intergranular stress generation in carbon steels. Acta Materialia **52**, 1937–1951 (2004)
36. Brode, H.L.: Blast wave from a spherical charge. Phys. Fluids **2**, 217–229 (1959)
37. Ivandaev, A.I., Kutushev, A.G.: Influence of screening gas-suspension layers on shock wave reflection. J. Appl. Mech. Technol. Phys. **26**, 103–109 (1985)
38. Kruglikov, B.S., Kutushev, A.G.: Attenuation of air shock waves by layers of dusty gas and lattices. J. Appl. Mech. Technol. Phys. **29**, 48–53 (1988)
39. Menikoff, R.: Detonation waves in PBX 9501. Combust. Theory Model. **10**(6), 1003–1021 (2006)
40. Toro, E.F.: A fast Riemann solver with constant covolume applied to the random choice method. Int. J. Numer. Methods Fluids **9**, 1145–1164 (1989)
41. Devals, C., Jourdan, G., Estivalezes, J.L., Meshkov, E.E., Houas, L.: Shock tube spherical particle accelerating study for drag coefficient determination. Shock Waves **12**, 325–331 (2003)
42. Igra, O., Takayama, K.: Shock tube study of the drag coefficient of a sphere in a non-stationary flow. Proc. R. Soc. Lond. A **442**, 231–247 (1993)
43. Clift, R., Grace, J.R., Weber, M.E.: Bubbles, Drops and Particles. Academic, New York (1978)
44. Sommerfeld, M.: The unsteadiness of shock waves propagating through gas–particle mixtures. Exp. Fluids **3**, 197–206 (1985)
45. Aizik, F., Ben-Dor, G., Elperin, T., Igra, O., Mond, M., Gronig, H.: Attenuation law of planar shock waves propagating through dust-gas suspensions. AIAA J. **33**(5), 953–955 (1995)
46. Chang, E.J., Kailasanath, K.: Shock wave interactions with particles and liquid fuel droplets. Shock Waves **12**, 333–341 (2003)
47. Rogue, X., Rodriguez, G., Haas, J.F., Saurel, R.: Experimental and numerical investigation of the shock-induced fluidization of a particles bed. Shock Waves **8**, 29–45 (1998)
48. Boiko, V.M., Kiselev, V.P., Kiselev, S.P., Papyrin, A.N., Poplavsky, S.V., Fomin, V.M.: Shock wave interaction with a cloud of particles. Shock Waves **7**, 275–285 (1997)